ADVANCING EARTH AND SPACE SCIENCE

JAMES | Journal of Advances in Modeling Earth Systems

RESEARCH ARTICLE
10.1029/2018MS001508

Key Points:
- Lagrangian particle dispersion is enhanced by smaller-scale flow features
- Lagrangian coherent structures are eroded in the presence of submesoscales and waves
- Satellite-derived velocities may overestimate the coherence of oceanic eddies

Supporting Information:
- Supporting Information S1
- Movie S1
- Movie S2
- Movie S3

Correspondence to:
A. Sinha,
as4479@columbia.edu

Citation:
Sinha, A., Balwada, D., Tarshish, N., & Abernathey, R. (2019). Modulation of lateral transport by submesoscale flows and inertia-gravity waves. *Journal of Advances in Modeling Earth Systems*, *11*, 1039–1065. https://doi.org/10.1029/2018MS001508

Received 22 SEP 2018
Accepted 23 FEB 2019
Accepted article online 28 FEB 2019
Published online 16 APR 2019

©2019. The Authors.
This is an open access article under the terms of the Creative Commons Attribution-NonCommercial-NoDerivs License, which permits use and distribution in any medium, provided the original work is properly cited, the use is non-commercial and no modifications or adaptations are made.

Modulation of Lateral Transport by Submesoscale Flows and Inertia-Gravity Waves

Anirban Sinha[1], Dhruv Balwada[2], Nathaniel Tarshish[3], and Ryan Abernathey[4]

[1]Applied Physics and Applied Mathematics Department, Columbia University, New York, NY, USA, [2]Courant Institute of Mathematical Sciences, New York University, New York, NY, USA, [3]Atmospheric and Oceanic Sciences Program, Princeton University, Princeton, NJ, USA, [4]Department of Earth and Environmental Sciences, Columbia University, New York, NY, USA

Abstract We investigate the role of small-scale, high-frequency motions on lateral transport in the ocean, by using velocity fields and particle trajectories from an ocean general circulation model (MITgcm-llc4320) that permits submesoscale flows, inertia-gravity waves, and tides. Temporal averaging/filtering removes most of the submesoscale turbulence, inertia-gravity waves, and tides, resulting in a largely geostrophic flow, with a rapid drop-off in energy at scales smaller than the mesoscales. We advect two types of Lagrangian particles: (a) 2-D particles (surface restricted) and (b) 3-D particles (advected in full three dimensions) with the filtered and unfiltered velocities and calculate Lagrangian diagnostics. At large length/time scales, Lagrangian diffusivity is comparable for filtered and unfiltered velocities, while at short scales, unfiltered velocities disperse particles much faster. We also calculate diagnostics of Lagrangian coherent structures:rotationally coherent Lagrangian vortices detected from closed contours of the Lagrangian-averaged vorticity deviation and material transport barriers formed by ridges of maximum finite-time Lyapunov exponent. For temporally filtered velocities, we observe strong material coherence, which breaks down when the level of temporal filtering is reduced/removed, due to vigorous small-scale mixing. In addition, for the lowest temporal resolution, the 3-D particles experience very little vertical motion, suggesting that degrading temporal resolution greatly reduces vertical advection by high-frequency motions. Our study suggests that Lagrangian diagnostics based on satellite-derived surface geostrophic velocity fields, even with higher spatial resolutions as in the upcoming Surface Water and Ocean Topography mission, may overestimate the presence of mesoscale coherent structures and underestimate dispersion.

Plain Language Summary Coherent structures represent the skeleton of fluid flow in the ocean, around which the large-scale transport of material gets organized. They usually manifest as (a) material trapping vortices that transport pollutants or biogeochemical tracers over long distances or (b) ridges of material transport barriers formed by regions of high fluid stretching. In this study, we investigate the role of small-scale/high-frequency motions on coherent structures, and more generally lateral transport in the ocean, by using velocity fields generated by a high-resolution ocean model. We average over the high-resolution velocity fields in time to smooth out the small-scale turbulent motions and use both the smoothed and unsmoothed velocities to advect virtual particles. For temporally smoothed velocity fields, we observe strong material coherence, which breaks down when the level of temporal smoothing is reduced/removed, as the high-frequency velocities scatter particles much faster. In addition, for the highest temporal smoothing, the particles experience very little vertical motion, suggesting that temporal resolution greatly affects vertical motion. Our study suggests that diagnostics based on satellite-derived ocean surface currents, even with higher spatial resolutions, as in the upcoming Surface Water and Ocean Topography mission, may overestimate the presence of coherent structures and underestimate small-scale scattering.

1. Introduction

Lateral mixing in the upper ocean plays an important role in Earth's climate system. For instance, near-surface lateral mixing processes help determine the ocean's rate of uptake of tracers such as heat and anthropogenic CO_2 (Abernathey & Ferreira, 2015; Balwada et al., 2018; Gnanadesikan et al., 2017;

Khatiwala et al., 2013; Liang et al., 2017; Marshall et al., 2017). Lateral mixing also strongly influences the global water mass distribution and overturning circulation (Groeskamp et al., 2017, 2018). Our ability to accurately model the ocean's impact on the global climate is consequently constrained by how effectively we parameterize lateral transport processes in the coarse-resolution models (Fox-Kemper et al., 2008; Gent & Mcwilliams, 1990; Gent et al., 1995; Grooms & Zanna, 2017; Marshall et al., 2017). In addition to influencing the large-scale circulation and tracer distribution, lateral mixing also plays a major role in controlling the structure of synoptic oceanographic processes such as pollutant dispersal on the surface ocean (e.g., oil spills and plastics; Mariano et al., 2011; Van Sebille et al., 2012) and local phytoplankton bloom evolution (Mahadevan, 2016; Mahadevan & Campbell, 2002; Martin, 2003).

Methods for characterizing lateral mixing and stirring in the ocean can be categorized broadly into two groups: analysis of spatial and temporal averages of dispersal (Davis, 1985, 1991; Okubo, 1971; Richardson & Stommel, 1948; Roach et al., 2016, 2018; Rypina et al., 2012; Marshall et al., 2006; Zhurbas & Oh, 2004) and identification of individual kinematic coherent flow features that might play a special role in transport. Absolute dispersion, relative dispersion, eddy diffusivity, scale-dependent relative diffusivities, and area-averaged finite-scale Lyapunov exponents are some of the commonly used metrics in the first category (see review by LaCasce, 2008). The latter category mostly falls under the umbrella of Lagrangian coherent structures (LCSs; see review by Haller, 2015). Spatial maps of finite-time Lyapunov exponents (FTLEs; Haller & Yuan, 2000), finite-scale Lyapunov exponent (d'Ovidio et al., 2009), geodesic transport barriers (Haller & Beron-Vera, 2013), and Lagrangian-averaged vorticity deviation (LAVD; Haller et al., 2016) are some of the commonly used LCS techniques. (Detailed descriptions of these diagnostics can be found in sections 3 and 4.)

The prevailing assumption is that mesoscale ocean flows, with horizontal scales of ~100 km and evolutionary times of months, are the dominant contributor to lateral stirring on scales relevant for the large-scale circulation and transport. Phenomenologically, the mesoscale is characterized by distinctive coherent structures such as vortices (i.e., eddies), fronts, and filaments. The relationship between these structures and the overall mixing rate is a matter of ongoing debate. For instance, Dong et al. (2014) and Zhang et al. (2014) both proposed, based on Eulerian methods, that trapping of fluid within coherent eddies and subsequent long-range transport is a major contributor to the overall mesoscale flux of mass and tracers. On the other hand, Wang et al. (2016) and Abernathey and Haller (2018), using objective Lagrangian methods, estimated that such coherent transport is only a small fraction of the total flux and that chaotic stirring occurring outside of eddy cores is the dominant transport mechanism. Despite their different conclusions, the studies above, and indeed a large fraction of all global-scale studies of the oceanic mesoscale, relied on satellite altimetry observations.

By enabling a global synoptic view of the mesoscale, satellite altimetry, and the associated geostrophic flow obtained by taking gradients of sea surface height (SSH) has transformed the field of oceanography fundamentally over the past 30 years (White, 2018). In particular, the AVISO (Archiving, Validation and Interpretation of Satellite Oceanographic data) gridded geostrophic velocity product (Ducet et al., 2000) is ubiquitous in recent studies of near-surface lateral transport (e.g., Abernathey & Haller, 2018; Abernathey & Marshall, 2013; Abraham & Bowen, 2002; Beron-Vera et al., 2008; Fu et al., 2010; Holloway, 1986; Keating et al., 2012; Klocker & Abernathey, 2014; Marshall et al., 2006; Poje et al., 2014; Shuckburgh & Haynes, 2003; Waugh & Abraham, 2008; Waugh et al., 2006, 2016). However, a new altimetry mission, the Surface Water and Ocean Topography (SWOT) satellite, is now on the horizon (Fu & Ferrari, 2008). This satellite will use a Ka-band radar interferometer to provide a high-resolution swath measurement of SSH, possibly providing useful data at spatial scales of 10 km or less (Fjortoft et al., 2014). The community is now grappling with the question of what this satellite will observe and what might be missing from our current generation of altimeters. In addition to the mesoscale, the SWOT SSH observations are expected to include significant signals from both submesoscale flows and inertia-gravity waves (IGWs). Submesoscale flows have been identified as playing a leading order role in providing a conduit for energy transfer toward microscale dissipation and diapycnal mixing (Capet et al., 2008; D'Asaro et al., 2011; McWilliams, 2016) and are also potentially important in controlling the rate of lateral spreading (Poje et al., 2014) and vertical transport (Klein et al., 2008; Omand et al., 2015; Rosso et al., 2016; Su et al., 2018) of tracers near the surface ocean. Inertial oscillations, tides, and IGWs are ubiquitous in high-frequency current measurements from moored instruments and surface drifters (Alford et al., 2016; Elipot et al., 2016; Ferrari & Wunsch, 2009). These higher-frequency flows project significant amount of kinetic energy (KE) on spatial scales comparable to those of the submesoscale flows (<50 km; Balwada, LaCasce, et al., 2016; Bühler et al., 2014; Callies et al., 2014; Rocha, Chereskin, et al., 2016).

The central goal of this contribution is to understand how motions from these different dynamical regimes and time scales influence Lagrangian transport in the near-surface ocean. A related question is, how reliable are transport estimates obtained from current and future satellite altimetry missions? Several past studies have examined these questions already. Beron-Vera (2010) calculated FTLEs from altimetry SSH observations as well as from a low-resolution ((1/4)°) and high-resolution ((1/12)°) HYCOM simulation. He found that the FTLE distribution and spatial pattern from the low-resolution model agreed well with the observations; however, the high-resolution model exhibited significantly different FTLE distributions and finer-scale structures. The conclusion was that while current-generation altimeters capture the large-mesoscale flow structure, quantitative estimates of trajectories and mixing rates would be improved by higher spatiotemporal resolution in the observing system. Several papers (e.g., Griffa et al., 2004; Poje et al., 2010) have studied the effect of spatial resolution on dispersion statistics using different models of varying complexity and reported that at large length/time particle dispersion is mainly controlled by energetic mesoscale features and are relatively insensitive to finer-scale motions. Taking a more idealized route, Keating et al. (2011) calculated dispersion in simple models of baroclinic turbulence and explored the dependence on the spatiotemporal sampling of the velocity fields. Lagrangian diagnostics that depend strongly on small scales, such as relative dispersion and FTLE, were found to be highly sensitive to spatial sampling. Temporal sampling error was found to have a more complicated behavior, with particle overshoot sometimes leading to scrambling of Lagrangian diagnostics. The nature of the turbulence itself (i.e., the slope of the KE wavenumber spectrum) strongly constrained the required sampling, with shallower spectra requiring more resolution. In addition to simulations, Lagrangian floats, which experience advection by the full flow, can be used to probe the limitations of satellite altimetry. For instance, Rypina et al. (2012) showed that the eddy diffusivity calculated from surface drifters in the North Atlantic was nearly twice of that estimated from synthetic drifters generated from satellite-altimeter-derived geostrophic velocity fields. They argued that Ekman flows alone do not explain the discrepancy, and small-scale unresolved geostrophic and ageostrophic velocities might be contributing to drifter-based eddy diffusivities being higher than those estimated from satellite fields. Similarly, Grand Lagrangian Deployment drifters have shown heightened dispersion by submesoscale motions in the vicinity of the Deepwater Horizon spill (Poje et al., 2014). Finally, in a more recent pair of papers, Beron-Vera, Hadjighasem, et al. (2018) and Beron-Vera, Olascoaga, et al. (2018) attempted to determine whether a Gulf of Mexico Loop Current eddy detected from AVISO-derived Lagrangian trajectories was truly materially coherent, given the possible presence of unresolved velocities in the AVISO product. Beron-Vera, Hadjighasem, et al. (2018) took advantage of a data-assimilating model of the region with 1-km grid spacing to produce virtual Lagrangian trajectories in the presence of a developed submesoscale field. The LAVD-based Lagrangian eddy detection method (Haller et al., 2016) was applied to these trajectories to extract the boundary of a coherent mesoscale structure with approximately the same position as the one identified from AVISO data. Beron-Vera, Olascoaga, et al. (2018) validated the existence of the same materially coherent eddy using drifters and ocean color observations. Haza et al. (2016) tested the robustness of LCSs derived from geostrophic currents at transport barriers by studying the evolution of a single mesoscale eddy (Star Eddy) in the Gulf of Mexico region. By comparing the full submesoscale resolving flow from a high-resolution ((1/100)°) regional simulation (HYCOM) with a spatially filtered flow approximating altimeter observations, the authors demonstrated that submesoscale motions can leak as much as 50% of the tracers out of a mesoscale eddy that preserves material under geostrophic flow. Since the earlier studies described above were conducted, a transformative new technology has emerged: ultrahigh-resolution global ocean models, which resolve, at least partially, the mesoscale, the submesoscale, the tides, and the IGW continuum. In the modeling studies of Beron-Vera (2010) and Keating et al. (2011), the advecting flow was assumed to be purely geostrophic, submesoscale motions were not resolved, and no tides were present. The models used by Haza et al. (2016) and Beron-Vera, Hadjighasem, et al. (2018) did permit submesoscale flow, but it encompassed only the Gulf of Mexico, a region where the dynamics is influenced, either directly or indirectly, by the Loop Current and the associated eddies. Here we examine the question of how different scales contribute to transport using a groundbreaking new global simulation with nonlocally forced tides and a realistic internal wave continuum, focusing on a much larger region, which includes the Agulhas and the Antarctic Circumpolar Current (ACC). We extract the velocity field from such a model, apply different levels of filtering, and calculate a range of Lagrangian mixing and transport diagnostics. This study can thus be seen as an update to an extension of prior work by Beron-Vera (2010), Rypina et al. (2012), Haza et al. (2016), and Beron-Vera, Hadjighasem, et al. (2018).

To filter out motions from different dynamical regimes, we apply *simple time averaging* to the velocity fields. Specifically, we take the raw velocity fields (sampled at hourly resolution) and average them over intervals of 1 day and 1 week. We do not explicitly apply any spatial filtering (e.g., Aluie et al., 2018), although the time averaging does result in smoother velocity fields (see section 3 for more details). Below are some of the reasons why we choose to examine time-averaged velocities:

1. Since different dynamical regimes (e.g., waves vs. balanced motions) are most reliably separated in time rather than in space (Wagner & Young, 2016), temporal filtering is a straightforward way to remove different processes from a given data set.
2. The SWOT science team has effectively adopted the daily averaged or 3-day-averaged flow as the "truth" signal for evaluating methods to separate balanced and unbalanced motions (Qiu et al., 2016, 2018; Wang et al., 2018).
3. Ocean model simulations commonly output time-averaged velocity fields such as daily, 5-day, or monthly averages.
4. The processing algorithms used to map along-track SSH observations to gridded maps (e.g., AVISO Ducet et al., 2000) involve some temporal smoothing.
5. Time averaging is computationally tractable even with very large data sets.

Although we are motived by the relevance to SWOT and other altimetry missions, our study is *not* an observing system simulation experiment; we have not attempted to reproduce the complex pattern of spatiotemporal sampling associated with real satellite observations. Rather, our focus is on the basic physics, for which time averaging is the most obvious filter. We are aware that more sophisticated methods exist for filtering waves and balanced motions (e.g., Barkan et al., 2017; Torres et al., 2018; Shakespeare & Hogg, 2017), but these methods are computationally infeasible for our data sets. Future studies may choose to employ the diagnostic framework described here, but with more sophisticated filters, for example, partitioning the flow into balanced motions and internal gravity waves based on the dispersion relation associated with the highest resolved baroclinic mode (Torres et al., 2018).

In this paper, we seek to answer the following three key questions: (1) How do fast–time scale velocities (subdaily and subweekly) affect near-surface lateral particle dispersion statistics? (2) How do these motions impact LCS? (3) What is the relative effect of the fast–time scale motions on vertical transport? The paper is organized as follows. In section 2, we introduce the llc4320 simulation velocity fields and examine the frequency and horizontal wavenumber power spectral density in our region of interest. In section 3, we describe the Lagrangian particle advection experiments used to calculate the different Lagrangian diagnostics. In section 4, we study the relative diffusivity from particle dispersion and discuss the potential implication for Lagrangian coherence. In section 5, we examine LCS via FTLE and LAVD. Section 6 summarizes the results and presents conclusions.

2. Model Domain and Power Spectra

We analyze model output from a primitive equation global ocean simulation that resolves mesoscale eddies, internal tides, IGWs, and other hydrostatic ageostrophic flows that may be present. The simulation analyzed here is the MIT general circulation model (MITgcm) lat-lon-polar cap 4320 (llc4320), which is the highest resolution ($(1/48)^\circ$) run in a hierarchy of simulations (Rocha, Chereskin, et al., 2016). The llc4320 simulation is based on a global ocean and sea ice configuration of the MITgcm, which was run with a time step of 25 s and with 90 vertical levels. The depth-based vertical grid varies in thickness from 1 m at the surface to 480 m near the bottom, with a maximum model depth of 7 km. (Control files and details of the high-resolution llc model setups and forcing files are available at http://mitgcm.org/viewvc/MITgcm/MITgcm_contrib/llc_hires.)

The model is forced at the surface with 6-hourly atmospheric fields from the 0.14° European Center for Medium-Range Weather Forecasts atmospheric operational model analysis, which, starting in 2011, is converted to surface fluxes using the bulk formulae of Large and Yeager (2004). The model also includes atmospheric pressure forcing and tidal forcing for 16 tidal constituents, which is applied to MITgcm as additional atmospheric pressure forcing. The details of the tidal forcing constituents used can be found in Savage et al. (2017).

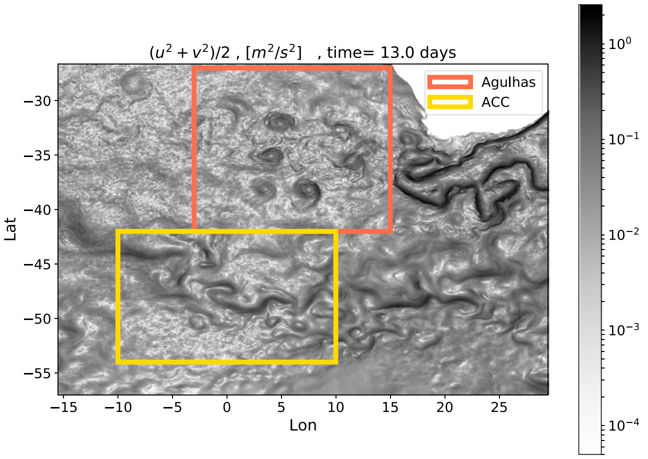

Figure 1. The domain with the specific subdomains used for the relative diffusivity calculation. A snapshot of the surface kinetic energy in the domain, with the Agulhas/Antarctic Circumpolar Current (ACC) regions marked in red/yellow. The relative diffusivity calculations (described in section 4) were done in these two regions separately to study dispersion characteristics of flows dominated by coherent eddies (Agulhas) and strong zonal shear (ACC).

This model develops a realistic tidal flow field and an IGW continuum that is reminiscent of the observed Garrett-Munk spectrum (Munk, 1981), which is thought to arise from nonlinear interactions between near-inertial waves driven by winds and internal tides generated by the interaction of the barotropic tide and topography. Savage et al. (2017), examining the frequency horizontal wavenumber spectra of dynamic SSH variance in both HYCOM ((1/12.5)° and (1/25)° resolutions) and MITgcm ((1/12)°, (1/24)°, and (1/48)° resolutions) simulations, reported that the choice of horizontal resolution affects the strength of the IGW continuum and that over most regions the higher resolution simulations captured the observed spectra more accurately at the higher frequencies (supertidal). They further showed that there are large peaks at the diurnal and semidiurnal frequencies in regions where diurnal and semidiurnal tides are known to be large.

The prognostic model variables were saved at hourly intervals as instantaneous snapshots (not averages). The use of instantaneous snapshots means that very high frequency (subhourly) oscillations may be aliased, potentially introducing spurious motion into the Lagrangian trajectories. We have no means to quantify this effect, other than by comparing with the temporally averaged velocity fields, for which any potential aliasing is smoothed away. We extract 73 days (starting from 13 September 2011) of hourly llc4320 model output from a broad region in the South Atlantic, which includes the Agulhas leakage and ACCs. The region spans (15.5°W to 29.5°E , 57°S to 26.6°S). A snapshot of the surface KE in the model domain is shown in Figure 1. This region exemplifies different regimes of flow, namely, strong shear flow in the ACC and coherent eddies in the Agulhas. Qualitatively, the ACC would be dominated by hyperbolic coherent structures and the Agulhas leakage by elliptic coherent structures (Haller, 2015).

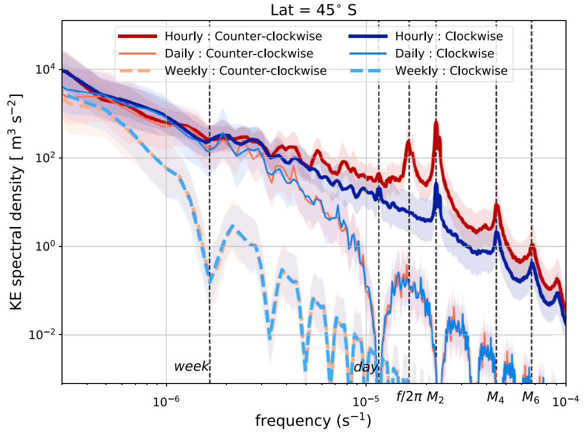

Figure 2. The frequency power spectral density (psd) of surface kinetic energy at 45°S for 73 days: The thick solid lines show the zonal mean (over 15.5°W to 29.5°E) of psd from the hourly velocities output by the MITgcm-llc4320. The thin lines corresponds to zonal mean of the psd calculated from the daily averaged velocities linearly interpolated to hourly intervals, and the thick dashed lines correspond to the weekly averaged velocities also linearly interpolated to hourly intervals. The shading denotes the 1 standard deviation error (across the longitude bands). The spectra are split into a clockwise (blue) and a counterclockwise (red) part by separating the positive and negative frequencies to isolate inertial oscillations. KE = kinetic energy.

In the following subsections we examine the frequency and wavenumber KE spectra to provide a sense of the relative amplitudes of the tides, IGWs, and balanced motions.

2.1. Time Averaging

As described in section 1, we employ time averaging of the velocity fields to filter out the fast time scales associated with tides, IGWs, and submesoscale flow. This is accomplished by grouping the *hourly* snapshots into *daily* and *weekly* blocks and taking the mean. This mean is representative of the time at the midpoint of each block. We refer to the daily and weekly averaged velocities generically as the *filtered velocities*. These three different velocity data sets constitute the main inputs to our analysis. The outputs are the different diagnostics described in subsequent sections.

2.2. Frequency Spectra

To assess how much energy is contained at different time scales, we calculate the rotary power spectrum of the surface velocities. The velocity is represented as complex valued time series, $\underline{u(t)} = u(t) + iv(t)$, for the 73-day period at each grid point. A Hanning window is applied to the time series before calculating the corresponding spectrum at each grid point, denoted by $\hat{u}\hat{u}^*(\omega)$, where $\hat{u}(\omega)$ is the Fourier transform of the complex valued time series, multiplied by a Hanning window. The power spectrum at each latitude is calculated by averaging the over the range of longitudes in the domain. The advantage of calculating the rotary spectrum is that the positive and negative frequencies correspond to the counterclockwise and clockwise motions. For the purpose of frequency spectral analysis, the filtered velocities as linearly interpolated in time back to the

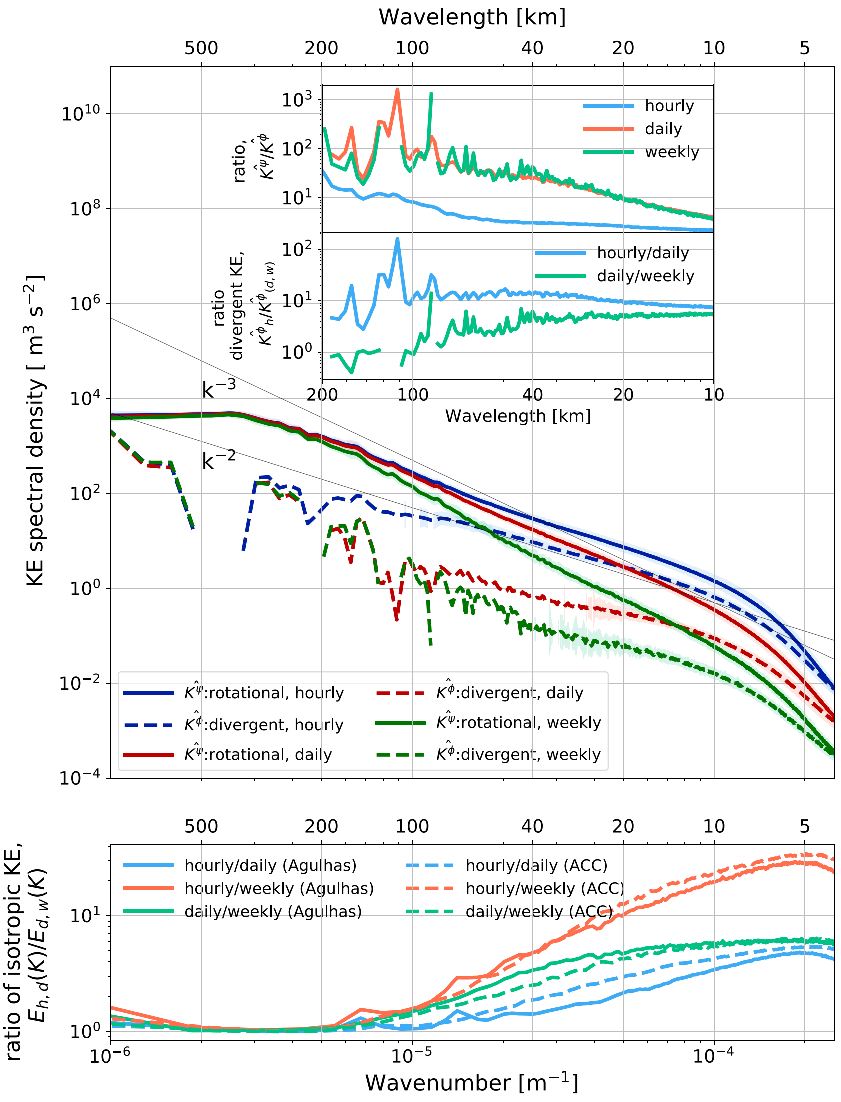

Figure 3. (top panel) Surface KE wavenumber spectra decomposed into the rotational (solid) and divergent (dashed) parts, (following Bühler et al., 2014) for the hourly velocities, daily averaged velocities, and weekly averaged velocities from the llc4320 numerical model simulations. (top panel, upper inset) The ratios of the rotational: divergent components. (top panel, lower inset) The ratios of hourly:daily (blue) and daily:weekly (green) divergent KE. (bottom panel) The ratios of the unfiltered (hourly) and filtered (daily, weekly) isotropic surface KE, calculated separately for the Agulhas and ACC sectors shown in Figure 1. The ratio of daily to weekly filtered velocities has also been shown for comparison. KE = kinetic energy; ACC = Antarctic Circumpolar Current.

original hourly temporal resolution, as this is how they are treated later when used for advecting Lagrangian particles.

We show the frequency power spectrum at 45°S latitude in Figure 2 as a representative, as the frequency spectra at different latitudes in the domain did not vary qualitatively. The spectrum is characterized by sharp peaks at frequencies greater than that corresponding to a day. The inertial oscillations ($\omega = \frac{f}{2\pi}$) and tides (M_2, M_4, M_6, and higher) are clearly visible. Savage et al. (2017) had shown that a few locations in the North Pacific, where McLane profiler observations were available, the tides in the modeled velocity time series were similar or greater in amplitude when compared to the observations.

In addition to inertial oscillations and tides, there is also a background level of power that presumably results from IGWs and balanced and ageostrophic flows. However, the frequency decomposition does not allow us to differentiate between these. In the next section we attempt to shed some light on the dynamics of the modeled flows by performing a decomposition of the wavenumber spectrum into rotational and divergent components.

The effect of time averaging is, unsurprisingly, to attenuate the signal power strongly above the averaging frequency. Time averaging plus linear reinterpolation is clearly not a perfect filter; however, residual high-frequency peaks and valleys remain in the filtered power spectra, with valleys corresponding to harmonics of the averaging time. While these stand out clearly on the log-log plot of Figure 2, we note that the power level at frequencies above the averaging frequency is everywhere smaller by at least a factor of 100 than the raw power level.

2.3. Wavenumber Spectra

In this section we investigate the wavenumber power spectra of the raw and filtered velocity fields. Further, we decompose these spectra into horizontally nondivergent and divergent components following a methodology described by Bühler et al. (2014). The mesoscale motions in the ocean are largely balanced/geostrophic, and hence nondivergent, while the tides, inertial oscillations, and IGWs project onto both the divergent and nondivergent parts of the horizontal flow. Submesoscale flows have a dominant balanced component, but at high Rossby number can have some projection onto the divergent component too (McWilliams, 2016). We also compare the effect of the temporal filtering on the wavenumber spectra of the surface KE under the Helmholtz decomposition. This helps us assess what fraction of the energy in the spectra at different scales is due to the nondivergent/rotational (mesoscale and balanced submesoscales) and divergent (tides, inertial oscillations, IGWs, and unbalanced submesoscale) flows.

We calculate the 1-D horizontal spectra along each latitude line in a subdomain spanning the full range of longitudes as in our domain but spanning ∼40–50°S in latitude for the surface velocity field. The top panel in Figure 3 shows the rotational (solid) and divergent (dashed) parts of the longitudinal (zonal) and transverse (meridional) KE spectra for the hourly unfiltered velocity (blue), daily averaged velocities (red), and weekly averaged (green) velocities. The thick lines represent the meridional mean of the 1-D Fourier decomposition along each latitude line from ≈(40–50°S), and the shading represents the one standard deviation error. We also calculated the power spectral density of isotropic surface KE ($E(K)$) in two smaller regions, spanning the Agulhas (3°W to 15°E, 42° to 27°S), and the ACC (10–10°W, 54° to 42°S; as shown in Figure 1) from the 2-D wavenumber spectra in these regions by integrating azimuthally over each K ($K = \sqrt{k^2 + l^2}$) in the wavenumber space.

$$E(K) = \iint_{k^2+l^2=K^2} E(k, l)\mathrm{d}k\mathrm{d}l. \tag{1}$$

The bottom panel in Figure 3 shows the ratio of unfiltered to filtered isotropic power spectral density at the surface. The red lines show the ratio of the power between hourly:weekly velocities ($E_h(K)/E_w(K)$) and the blue lines correspond to hourly:daily velocities ($E_h(K)/E_d(K)$).

The spectra are mostly flat at large scales and start dropping off at scales smaller than 200 km. The drop-off in energy at length scales smaller than 10 km is very rapid, presumably a result of the viscous dissipation. In the discussion here, we restrict our attention to the 10- to 200-km range, which is influenced by the temporal filter but not strongly influenced by dissipation. We observe a consistent decrease in power with filtering in both the rotational and divergent components at length scales smaller than ∼100 km. This is an indication that the high-frequency motions filtered out by time averaging are primarily associated with small spatial scales. The nondivergent component of the spectra is more energetic than the divergent component, even for the unfiltered velocities. The ratio of the nondivergent to divergent energy increases with low-pass filtering (top panel, upper inset, Figure 3). The difference of the divergent KE between the hourly unfiltered and daily filtered KE is larger than the difference of divergent KE between daily and weekly filtered KE at all intermediate length scales (lower inset, top panel). This indicates that the superinertial motions have a large divergent component. The isotropic KE is 30 times lower for the weekly filtered velocities and 3 times lower for the daily filtered velocities at the smallest scales (<10 km). This indicates that while at intermediate scales, the daily filter removes most of the divergent KE, the total KE loss is much greater going from the daily filter to the weekly filter. At the smallest scales, similar amounts of energy are lost at each successive filtering.

The spectral slope for the rotational component of the unfiltered velocity field roughly follows a k^{-3} power law in the 50- to 200-km range and flattens out to k^{-2} at smaller length scales. These slopes are in general

Table 1
Lagrangian Particle Advection Experiments Carried Out

Experiment	Hourly velocities	Daily averaged velocities	Weekly averaged velocities
3-D particles	3D-h	3D-d	3D-w
2-D particles	2D-h	2D-d	2D-w

agreement with theoretical expectations and what has been observed in previous modeling studies. The k^{-3} slope is reminiscent of the forward enstrophy cascade in geostrophic turbulence (Charney, 1971). The exact origin of k^{-2} slope observed at small scales is still a matter of debate but is believed to be orchestrated by a combination of mixed layer baroclinic instability (Boccaletti et al., 2007), surface quasi-geostrophic modes (Lapeyre & Klein, 2006), and intertia-gravity waves (Bühler et al., 2014; Callies & Ferrari, 2013). The corresponding divergent component of the unfiltered velocity follows approximately a k^{-2} at all length scales. With temporal filtering the power of the divergent component is reduced, but the spectral slope is relatively uninfluenced. However, the spectral slope of the nondivergent component of energy becomes steeper with temporal filtering, getting close to k^{-3} power law in the 10- to 200-km range with the weekly temporal filter. This suggests that the weekly filtered velocity fields, where the influence of the fast ageostrophic flows has been removed, are smooth and might be kinematically similar to interior-quasi-geostrophic dynamics (Le Traon et al., 2008; Keating et al., 2011).

3. Off-Line Lagrangian Particle Advection Experiments

The goal of this work is to understand the lateral transport mechanisms that are active in the surface ocean. We use numerical particles to elucidate the influence of the Eulerian flow field on the Lagrangian transport. We employ the off-line mode (Abernathey & Marshall, 2013) of the MITgcm, where the dynamical core is disabled, and we use the filtered/unfiltered velocity fields for our region, taken from the MITgcm-llc4320 simulations as described in the previous section, to advect Lagrangian particles injected at the surface. The off-line model uses a fourth-order Runge-Kutta advection scheme for the particles (no tracer advection) and multilinear interpolation in space and time. We set up experiments with two kinds of particles: 2-D and 3-D. The 2-D particles are restricted to stay at the surface layer and are advected only by the horizontal component of the surface velocity, while the 3-D particles are allowed to be advected by the full three-dimensional velocity field. The 3-D particles are most representative of the true Lagrangian trajectories, while the 2-D particles can be thought of as the approximate trajectories of inertial particles whose strong buoyancy effectively constrains them to remain close to the sea surface (Maxey & Riley, 1983), similar to surface drifters. The 3-D particles can give us some insight into the influence of the strong vertical velocities (that are often seen in high-resolution simulations; Choi et al., 2017; Klein & Lapeyre, 2009) on Lagrangian transport and shed light on the limitations of assuming 2-D geostrophic flow.

Table 1 summarizes the six experiments conducted for our present study and the shorthand we will use for referring to these experiments. Here the 2D-w experiment represents the case that is closest to Lagrangian particle advection using satellite altimetry-derived velocities, which have a nominal temporal resolution of 7–10 days. As noted in section 1, none of these cases should be considered an observing system simulation, since the sampling and processing behind real satellite altimetry products is considerably more complex than simple time averaging. If we were to arrange these experiments in order of most to least realistic, the closest to the “real” ocean would be the 3D-h case, and the least realistic, and the closest to geostrophic trajectories inferred from satellite altimetry, would be the 2D-w case, with realism decreasing downward and right in Table 1. Surface drifter experiments (Lumpkin & Johnson, 2013) are closest to the 2D-h case, as drifters do not track the fluid vertically.

In each case, the particles are initialized on a regular horizontal grid spacing of $(1/100)^\circ \times (1/100)^\circ$ at the surface, a total of $4,450 \times 2,900$ particles. For each of the simulations, when a particle reaches the edge of the domain, it stops moving due to the imposed boundary conditions and therefore “dies.” We remove the “dead” particles from the analysis that is performed in this study to ensure that all trajectories used here are of the same temporal length. This effectively creates a spatial mask (seen in Figure 6) over the domain.

For comparison with some (but not all) diagnostics, we also computed particle trajectories in the Agulhas region (15.5°W to 29°E, 56–26°S, roughly the same region as our Agulhas sector for llc) from a previous

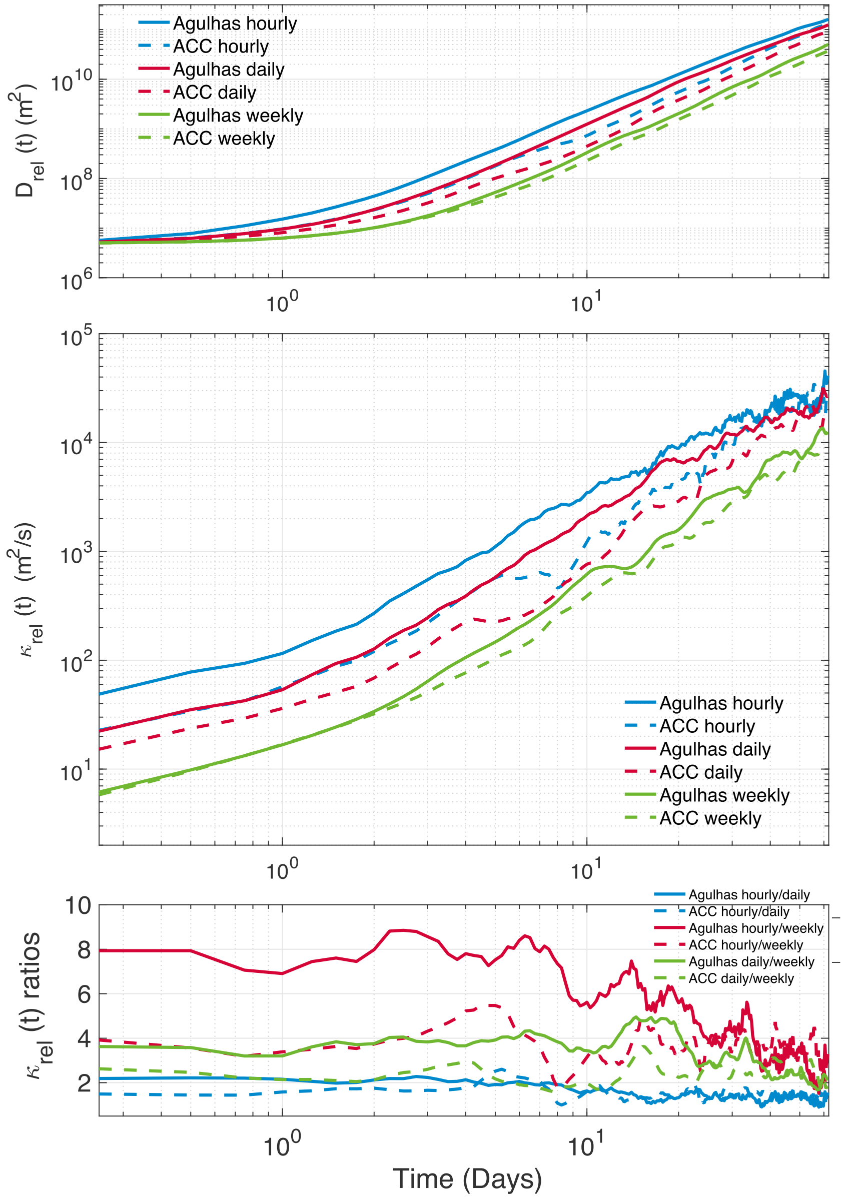

Figure 4. Surface relative dispersion (top), relative diffusivities (middle), and ratios of the relative diffusivities (bottom) as a function of time, in the Agulhas (solid) and the ACC (dashed), for the three 2-D experiments. ACC = Antarctic Circumpolar Current.

MITgcm off-line simulations for the entire globe. In this global off-line simulation, particles were initialized on a (1/32)° horizontal grid and had the trajectories output daily. The details of the MITgcm off-line simulations with AVISO velocities can be found in Abernathey and Haller (2018).

In the following sections we describe the characteristics of the Lagrangian transport, using relative dispersion statistics and Lagrangian coherence, that is experienced by the particles in the different experiments.

4. Relative Dispersion and Diffusivity

Dispersion is one of the most basic metrics that can be used to quantify the influence of turbulent motions on transport. Similarly to the variance, it gives a measure of the size of a group of particles. Generally, dispersion is measured as the absolute dispersion, relative to the initial release point of particles, or the relative dispersion, relative to the evolving center of mass of the group of particles. In the absence of a background mean flow and for Brownian/uncorrelated motion, absolute dispersion and relative dispersion are the same.

However, in more complex flows like in the ocean, relative dispersion provides a better measure of the spread of particles by turbulence alone and is not influenced by mean advection. Babiano et al. (1990), Bennett (1984), LaCasce (2008), and Foussard et al. (2017) provide excellent reviews of relative dispersion and theoretical relationships for inertial ranges of 2-D turbulent flows. Here we use relative dispersion as a measure to see how the bulk transport properties change with time-averaged velocity fields.

Relative dispersion (D_{rel}) is defined as the mean squared separation over all particle pairs, where the choice of pairs provides a conditional averaging. Here we define pairs as all particle combinations that were initially separated by distance r_o.

$$D_{\mathrm{rel}}(t, r_o) = \frac{1}{2N(N-1)} \sum_{i \neq j; |\mathbf{X}_i(0) - \mathbf{X}_j(0)| = r_o} |\mathbf{X}_i(t) - \mathbf{X}_j(t)|^2, \tag{2}$$

where N is the number of particles that contributed to forming pairs and $\mathbf{X}_i$ and $\mathbf{X}_j$ are position vectors of the two particles in the pair. A corresponding relative diffusivity, the rate of separation growth, can be defined as

$$K_{\mathrm{rel}}(t, r_o) = \frac{1}{2} \frac{\mathrm{d}}{\mathrm{d}t} \left(D_{\mathrm{rel}}(t, r_o) \right). \tag{3}$$

We can also, albeit coarsely, relate the relative diffusivity to a length scale by performing a change of variables from time to separation scale (r), where the separation scale is defined as the square root of the relative dispersion. Applying the change of variables, we obtain an expression for the relative diffusivity with r as the independent variable:

$$K_{\mathrm{rel}}(r, r_o) = K_{\mathrm{rel}}(r = D_{\mathrm{rel}}(t, r_o)^{\frac{1}{2}}, r_o). \tag{4}$$

Two regions—Agulhas (3°W to 15°E, 42° to 27°S) and ACC (10–10°W, 54° to 42°S)—were chosen for calculating the relative dispersion and diffusivity from the simulations with the filtered and unfiltered velocities (as shown in Figure 1). We chose r_o to be the grid separation (~2 km) at which all particles were initially released, as this allows the turbulent transport to be sampled down to the smallest length scales in the system. Except for the differences in magnitude, the two regions exhibit qualitatively similar behavior. Therefore, unless otherwise noted, the following discussion applies equally to both regions.

In Figure 4, the relative dispersion, the relative diffusivity and the ratios of relative diffusivities for the particles advected by the unfiltered and filtered velocities are plotted as a function of time in the two sectors. The unfiltered hourly velocities disperse particles faster and farther than the daily or weekly filtered velocities. At small time, <5–10 days, the diffusivity calculated from the rate of change of dispersion is small, $O(100\ \mathrm{m^2/s})$ and increases by 2–3 orders of magnitude with time for both filtered and unfiltered velocities. This increase in diffusivity can be understood as a result of the larger, more energetic eddies starting to play a more dominant role in dispersion at longer times. At times longer than those analyzed here, approximately 150 days, the motion of the particle pairs will decorrelate and the diffusivity will saturate to the eddy diffusivity corresponding to that for the largest eddies in the flow (Balwada, Speer, et al., 2016; LaCasce, 2008, 2014). The smaller eddies in the unfiltered velocity fields are able to spread particles apart more rapidly than the filtered velocity fields, allowing the influence of the larger eddies to be felt sooner.

The relative diffusivity is the largest for the unfiltered hourly velocity fields. The ratio of the hourly to weekly diffusivities goes from 8 at small times to ~3 at the end of the simulation period (~60 days) in the Agulhas. In the ACC, the diffusion by hourly velocities is 3–5 times higher than the weekly velocities at all times, and the relative magnitude does not decay post ~10 days. The absolute magnitudes of the relative diffusivity at initial times are also smaller for the ACC compared to the Agulhas region. This is an indication that the smaller eddies, which influence the dispersion initially, in the ACC are weaker or less efficient at dispersing particles than in the Agulhas. This might be due to one or both of the following reasons: (a) The scales of submesoscale might just be smaller in the ACC and so are not resolved in the llc4320 or (b) the presence of a strong mean flow suppresses the growth of the submesoscale modes (Taylor et al., 2018).

It should also be noted that the difference in tracer spreading between the hourly and daily velocity fields is smaller than the difference between the daily and weekly. This is to be expected as we damp out a larger fraction of the KE with a longer time filter (see Figure 2). However, this is also an indication that tidal and wave motions, which are present only at time scales smaller than 1 day, are less efficient at inducing

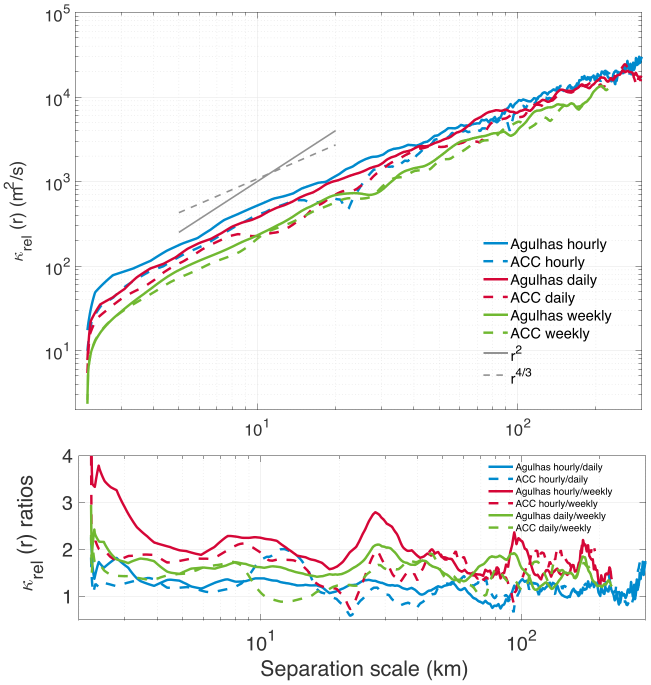

Figure 5. Surface relative diffusivities (top) and ratios of the diffusivities (bottom) in the Agulhas (solid), and the ACC (dashed), for the three 2-D experiments as a function of the mean separation ($D_{\mathrm{rel}}^{1/2}$). ACC = Antarctic Circumpolar Current.

turbulent transport than submesoscale turbulent flows. Small-amplitude linear waves in a homogeneous background would indeed be expected to cause zero dispersion.

An alternate perspective to the time domain is to look at the relative diffusivity as a function of separation length scale (equation (4) and Figure 5). From this perspective, the difference between the turbulent transport by hourly unfiltered and daily filtered velocity is less: The relative diffusivity due to the hourly velocity fields is only about 20–30% greater than the daily filtered velocity fields at small length scales and almost indistinguishable at large length scales. The relative diffusivity for the weekly velocity field is about half the size of the hourly velocity field. The reason for this difference is that the mapping from $K_{\mathrm{rel}}(t)$ to $K_{\mathrm{rel}}(r)$ uses the dispersion D itself to define the length scale, which means that, at a given value of r, we are comparing dispersion from the different experiments at different times in the particle evolution. This collapses the distinct curves of Figure 4 into a much tighter relationship.

This section has shown that fast–time scale motions make a considerable contribution to mixing, particularly at small scales but also at scales of hundreds of kilometers and months. Such fast time scales are absent from current generation altimetry-derived velocity products. Thus, in agreement with Rypina et al. (2012) and Beron-Vera (2010), we conclude that altimetry-inferred mixing diagnostics in the upper ocean may underestimate dispersion significantly. This enhanced mixing at small scales by high-frequency velocities can be explained, at least qualitatively, by the influence of reduced KE at small length scales (seen in Figure 3). In addition, we also note that the spectral slopes are steeper in the ACC than the Agulhas region (not shown in the figures), indicating weaker overall submesoscale energy and correspondingly a relatively smaller influence on dispersion. It appears that we are likely to underestimate lateral mixing at small scales by a factor of at least 2, dependent on the region of the ocean, if we neglect the fast time scales. A factor of 2 discrepancy was also observed (Rypina et al., 2012) between diffusivity estimates from drifters and satellite altimetry in the North Atlantic.

While relative dispersion and diffusivity provide bulk estimates of differences in turbulent transport, they do not provide a detailed picture of the mechanisms at work in the dispersion of particles. Further understanding can be developed by looking at the details of the kinematics. In the subsequent sections we examine how small scales can affect Lagrangian coherence, by studying different Lagrangian coherent structure diagnostics in the presence and absence of these high-frequency motions.

5. Lagrangian Coherence Diagnostics

A visual survey of the ocean mesoscale suggests the presence of structures in the flow, rather than a random diffusive transport. These structures, which often show coherent motion in space and time, are referred to as LCSs (see review by Haller, 2015). There exist a plethora of different methods for detection of LCSs. Hadjighasem et al. (2017) present a very detailed summary of the various existing diagnostics in the context of idealized 2-D turbulence examples. Each of these methods has its merits and drawbacks. For our study we have chosen to focus on two of these methods—FTLEs and LAVD. FTLE has been around for quite some time as a method for detecting material transport barriers and is useful for detecting jets and other strong shear flows (attracting and repelling hyperbolic LCSs; Haller, 2002; Pierrehumbert & Yang, 1993). On the other hand, the recently devised LAVD method has been shown to be a robust, objective method for detecting materially bounded vortices (elliptic LCSs; Beron-Vera, Hadjighasem, et al., 2018; Haller et al., 2016). As such, FTLEs and LAVD serve as complementary methods for detecting different types of LCSs.

5.1. FTLE

Many previous studies (e.g., Beron-Vera et al., 2008; Keating et al., 2011; Waugh & Abraham, 2008; Waugh et al., 2006, 2012) have computed FTLEs from the advection of Lagrangian particles with ocean velocity fields. We briefly review the basic theory in the following paragraphs following Haller (2011) and

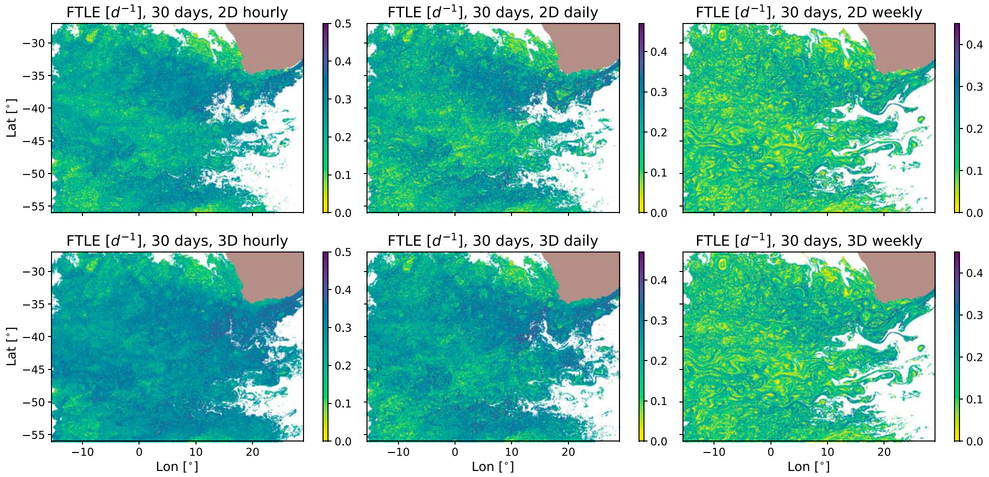

Figure 6. Finite-time Lyapunov exponents (FTLEs) after 30 days, for Lagrangian particles in the Agulhas sector advected by hourly velocities (left), daily averaged velocities (middle), and weekly averaged velocities (right) from the llc4320 numerical model simulations. The top panels are for the 2-D particles, and bottom panels are for 3-D particles. The mask (white) represents the initial positions of all particles that reached the edge of the domain at the end of the integration. Land is represented by the brown mask.

Farazmand and Haller (2012). For Lagrangian particles initially located at (x_0, y_0) at time t_0 and advected to (X, Y) at time t, the flow map at time t as a function of their instantaneous position is

$$\mathbf{F}^t_{t_0}(x_0, y_0) := \left(X(x_0, y_0, t), Y(x_0, y_0, t)\right) \tag{5}$$

From the flow map $\mathbf{F}^t_{t_0}$ we calculate the Jacobian as $\nabla\mathbf{F}^t_{t_0}(x_0, y_0)$. Then, the right Cauchy-Green stress tensor $\mathbf{C}^t_{t_0}$ is calculated as

$$\mathbf{C}^t_{t_0}(x_0, y_0) = \left(\nabla\mathbf{F}^t_{t_0}(x_0, y_0)\right)^T \nabla\mathbf{F}^t_{t_0}(x_0, y_0) \tag{6}$$

This symmetric, positive definite tensor, $\mathbf{C}^t_{t_0}(x_0, y_0)$ admits two real positive eigenvalues, λ_i and real orthogonal eigenvectors, ξ_i, defined by

$$\mathbf{C}^t_{t_0}(x_0, y_0)\xi_i = \lambda_i \xi_i, \quad \|\xi_i\| = 1, \quad i = 1, 2$$

and

$$0 < \lambda_1 \leq \lambda_2$$

where λ_i and ξ_i are functions of (x_0, y_0, t). The maximum eigenvalues of this Cauchy-Green tensor, λ_2, give the forward time FTLE as follows:

$$\text{FTLE} = \frac{1}{t - t_0}\log(\lambda_2). \tag{7}$$

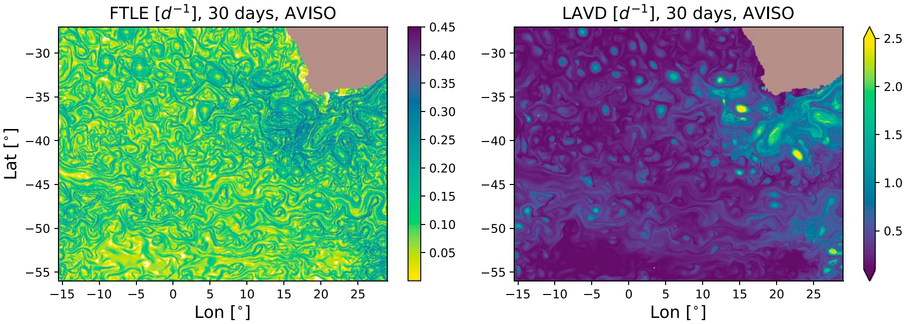

Figure 7. (left panel) Finite-time Lyapunov exponents (FTLEs) and (LAVD) Lagrangian-averaged vorticity deviation (right panel) for particles advected by AVISO velocities after 30 days, shown for the Agulhas sector. The brown mask represents land.

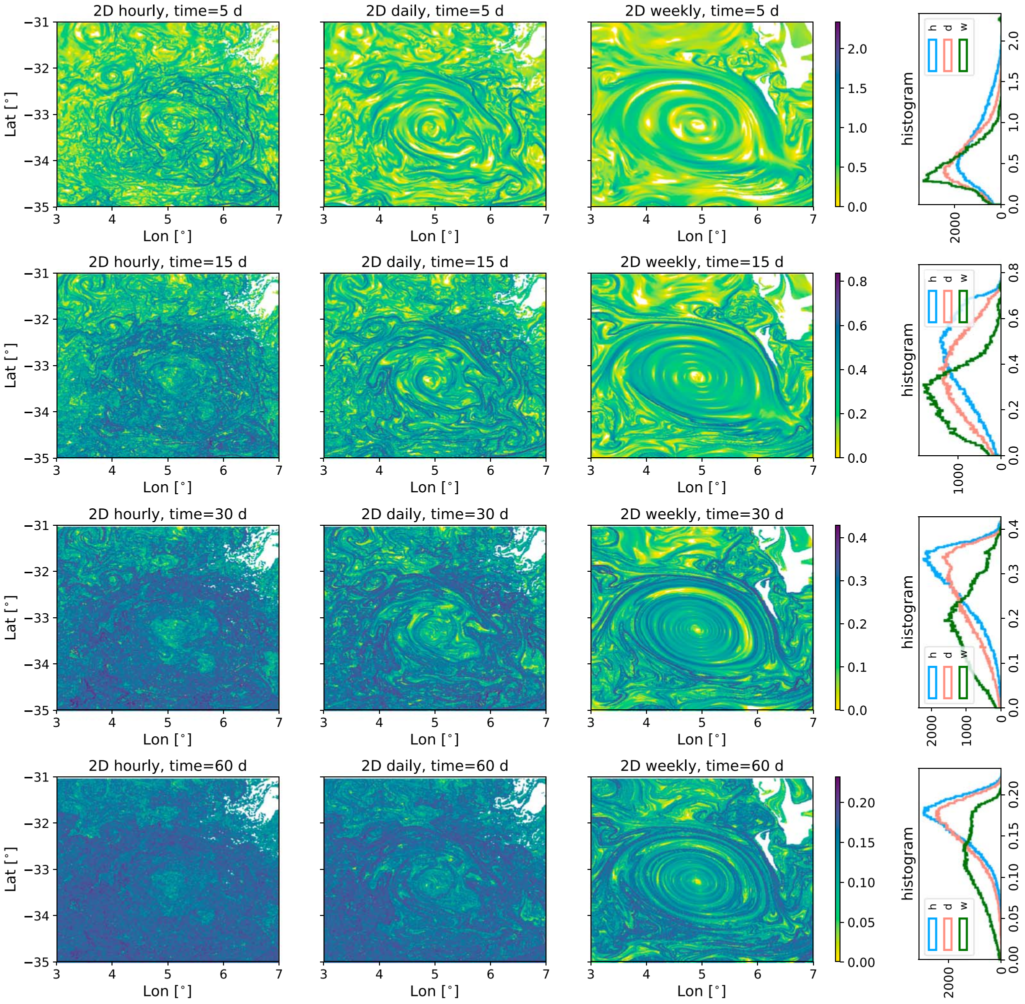

Figure 8. Snapshots of the finite-time Lyapunov exponent (FTLE) field, zoomed in, near an eddy at different times, for the three 2-D particle advection experiments with filtered and unfiltered llc4320 velocities. Note that the color bars are different for different times. The max/min limits of the color bar for each time step is chosen to represent the max/min FTLE values at that time. The right-hand panels show the histogram of FTLE in this box. The distribution shows that at long times, for daily and hourly velocities the FTLE is more strongly peaked at higher values compared to the weekly velocities.

For each time t, (7) provides a measure of material stretching of a fluid parcel (integrated strain and divergence along the trajectory of each particle) for the time period $t - t_0$ and can be plotted at the initial position (x_0, y_0) of each particle. Similarly, the backward time FTLE at the location $(X(x_0, y_0, t), Y(x_0, y_0, t))$ can be calculated as the negative of the logarithm of the smallest eigenvalue λ_1 of $\mathbf{C}_{t_0}^{t}(x_0, y_0)$ at the initial position (x_0, y_0; Haller & Sapsis, 2011). Unless otherwise mentioned, we refer to the forward time FTLE, mapped at the initial positions (x_0, y_0), as FTLE in this study. In Figure 6, the FTLE after 30 days is shown for each of the six experiments described in Table 1.

We also consider the 30-day FTLE fields, for particles advected with AVISO velocities in Figure 7 (left panel) for comparison. The FTLE field shown is for the region (15.5°W to 29°E , 56°S to 27°S), the same region as our Agulhas sector for llc. We note that although the FTLE shown for the AVISO is for a 30-day period, it is not the same 30-day period, so we are not offering a direct comparison here. Also, as opposed to our simulations where we had to impose boundary conditions on the limited domain under consideration, the AVISO particle simulation was done on the entire globe and thus does not show masked out regions corresponding to particles that left the domain.

We observe that the FTLE field from the AVISO velocities is qualitatively very similar to the FTLE field from the llc model experiments with the weekly averaged velocities. When we compare the two panels on

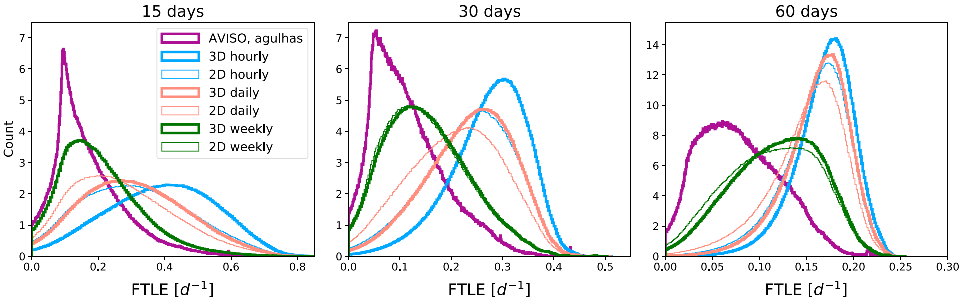

Figure 9. The distribution of the finite-time Lyapunov exponent (FTLE) probability density function for the six particle advection experiments with filtered and unfiltered llc4320 velocities along with the FTLE distriution for the particle tracking experiment with AVISO velocity fields in the Agulhas sector.

the right of Figure 6, with the left panel in Figure 7, we notice the maxima of FTLE to be the same order of magnitude and distributed similarly in the domain in both these figures. In addition, the coherent patterns traced out by the high FTLE ridges have roughly the same length scales. This is not surprising, since, by filtering out time scales smaller than a week, we are effectively reducing the resolution of the llc model to that obtained from AVISO.

We start with a qualitative description of the structures observed in the FTLE maps and examine the sensitivity of FTLE to the time interval. The FTLEs (zoomed in near a coherent mesoscale eddy observed in 2Dw) at 5,- 15-, 30-, and 60-day periods, for the three 2-D experiments are shown in Figure 8. The ridges (maxima) of FTLE represent regions of high fluid strain, which may act as material transport barriers. We observe that these ridges are long, smooth, and well defined only for weekly filtered velocities at long times. At short times (<15 days), clear, well-defined fine-scale FTLE ridges are observed for the hourly and daily averaged velocities, revealing a strong submesoscale signature. At times longer than 30 days, for the daily velocities, we observe few such narrow ridges of high FTLE. However, at such long time scales, due to vigorous mixing at small scales by the hourly velocities, the large-scale patterns of FTLE traced out by the mesoscale eddy are completely engulfed by the small-scale features and the FTLE field appears blurry. This finding is somewhat different from Beron-Vera (2010), who found that high-resolution ((1/12)°) SSH-inferred geostrophic velocities produced FTLE fields with very intricate fine-scale structure, which was still discernible. Our experiments use a higher-resolution model velocity field with a strong unbalanced component, and as a result, vigorous mixing by submesoscale turbulent flows and IGWs evidently leads to complete scrambling of coherent FTLE ridges. For the weekly filtered velocities, there is little qualitative difference as the time period is changed, but the overall magnitude of the FTLE value decreases.

A useful quantitative way to assess the effect of filtering on the FTLEs is via their distributions. The probability density functions (PDFs) of the same FTLE fields are shown in Figure 9. For comparison, we also show the 30-day FTLE fields from a similar region produced from AVISO surface geostrophic velocities (starting from 1 January 1993). As discussed by Beron-Vera (2010), an FTLE PDF with a long tail suggests that most of the mixing in the flow is accomplished in a few special regions of strong stretching (such as coherent filaments). In contrast, a more Gaussian PDF indicates that a range of structures at all scales contributes to mixing. Beron-Vera (2010) found that FTLEs from AVISO (calculated for different 30-day periods between 3 March 2008 and 8 March 2009) and those from a (1/4)° model exhibited a very similar PDF, which peaked between 0 and 0.1, with a long tail extending to larger values.

As shown in Figure 9, in strong contrast to the AVISO distribution, the FTLE from both the hourly and daily experiments is skewed toward high values, with peaks in the range of 0.2–0.3 at long times ($t \geq 30$ days). Daily filtering shifts the distribution somewhat toward lower values, but only weekly filtering induces a qualitative change; the weekly PDF is more symmetric and peaks close to 0.1. The mode value of FTLE for AVISO velocities is shifted even further left than the weekly velocities. This again is in agreement with the hypothesis that satellite altimetry is similar to the 2D-w corner of Table 1. At short times ($t \leq 30$ days) the weekly and the daily velocity FTLE pdf is skewed toward low values but still higher than the AVISO. None of the PDFs diagnosed from our experiments displays a skewness similar to the AVISO-derived FTLE, whose PDF peaks around 0.05. This means that the mixing process in the llc simulation is generally more intense and homogeneous. This finding is somewhat similar to Beron-Vera (2010), who showed that the distribution of FTLE

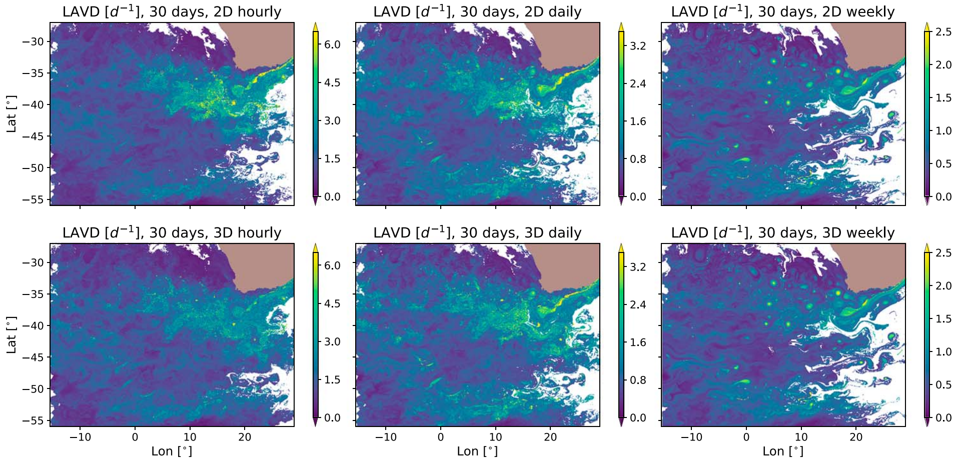

Figure 10. Lagrangian averaged vorticity deviation (LAVD) integrated after 30 days, for Lagrangian particles in the Agulhas sector advected by hourly velocities (left), daily averaged velocities (middle), and weekly averaged velocities (right) from the llc4320 numerical model simulations. The panels on the top are for the 2-D particles, and the panels on the bottom are for 3-D particles. The white mask represents the initial positions of all particles that reached the edge of the domain at the end of the integration. The brown mask represents land.

was skewed toward higher growth rates when high-resolution ((1/12)°, HYCOM) velocities (computed from SSH) were used to advect particles and toward low values when low-resolution (interpolated to (1/4)°) velocities were used. In addition, at short times (≤30 days), the hourly and daily averaged FTLE distributions are markedly different from each other; however, at long times (60 days), they almost overlap. This arises due to the scrambling of the FTLE ridges by vigorous submesoscale mixing in the hourly and daily averaged cases at long time scales (partially attributable to the particle resolution being insufficient to capture the very narrow filaments at such long time scales), which causes higher overall FTLE values (Figure 10). This is markedly different from the weekly averaged case where such strong submesoscale motions are absent.

Furthermore, vertical motion strongly affects the character of the FTLE ridges. When the fastest time scales are considered, there is significant difference between the FTLE fields between particles that are restricted to one vertical plane and particles that are advected in three dimensions. This difference is more clearly seen in the PDF of the FTLE for the 2-D and 3-D particles. With hourly velocities, the distribution differs markedly between 2-D and 3-D particles; with the 2-D particles having smaller FTLE overall, the distribution is flatter. This difference decreases for the daily averaged velocities, and the 2-D and 3-D FTLE distributions are almost exactly the same for the weekly averaged velocities. This shows that, by filtering out faster–time scale processes, we are also filtering out vertical motions associated with these fast time scales.

FTLE tells us about strain rates in the flow field, which represents one kind of coherence, namely, material transport barriers due to fluid stretching. As we get further away from the satellite altimetry (nondivergent) like velocity fields and get closer to velocity fields with unbalanced flows (as we might expect with a more realistic representation of the ocean), we observe higher and smaller-scale strain in the domain.

In the next section, we describe the methodology used to detect materially bounded eddies (coherent Lagrangian vortices) from our Lagrangian particle advection experiments and investigate the role of temporal filtering on the presence or absence of these structures.

5.2. LAVD

The role of coherent mesoscale eddies in ocean transport is currently a topic of great interest and debate. Do such eddies trap material and transport it over long ranges, without exchange with the outside environment, or are they “leaky?” Agulhas rings are perhaps the best known example of such coherent eddies (Beron-Vera et al., 2013; Van Sebille et al., 2012), which partly motivated the choice of our study region. In the following paragraphs, we describe a method for objectively detecting such coherent vortices and then describe how this method was applied to the llc velocity data set.

There have been numerous Eulerian and Lagrangian techniques developed to attempt to identify coherent mesoscale eddies (e.g., Beron-Vera et al., 2013; Chelton et al., 2007; d'Ovidio et al., 2009; Faghmous et al.,

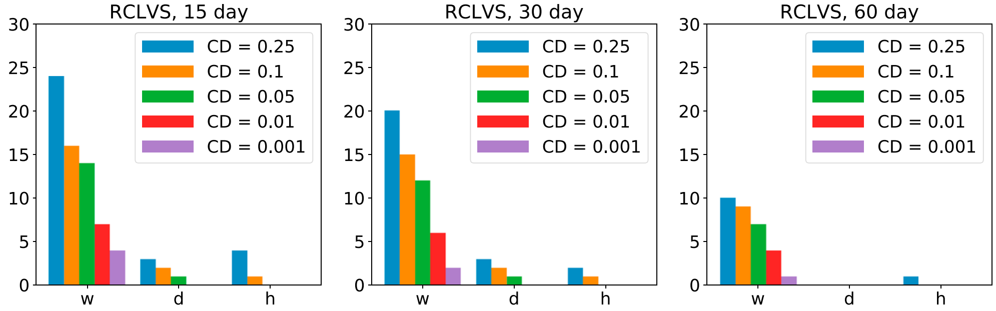

Figure 11. Number of rotationally coherent Lagrangian vortices (RCLVs) detected in the domain for the different 2-D experiments (h = hourly; d = daily; and w = weekly) at different times for different choices of convexity deficiency (CD). The minimum area required for the algorithm to detect an RCLV was set to 400 km^2, and the minimum allowable distance between two RCLVs was set at 100 km.

2015; Haller, 2002; Haller & Beron-Vera, 2013; Haller & Yuan, 2000; Haller et al., 2016; Isern-Fontanet et al., 2003, 2006; Morrow et al., 2004). Here we apply the recently developed method of Haller et al. (2016) based on Lagrangian-averaged vorticity. The physical essence of this method is that it searches for compact regions of the fluid, which experience similar rotation over their lifetime—this definition fits well with most oceanographers' intuitive understanding of a vortex or eddy.

Our method and numerical approach to identifying such eddies is identical to the one described in Abernathey and Haller (2018). We begin with the instantaneous two-dimensional relative vorticity, ζ, defined by

$$\zeta = -\frac{\partial u}{\partial y} + \frac{\partial v}{\partial x} \quad . \tag{8}$$

In our experiments, the vorticity is calculated from the input velocity fields and interpolated linearly in space and time to the positions of all the Lagrangian particles. To maintain the frame invariance of the method (Haller et al., 2016), it is necessary to remove any solid body rotation. For that purpose, the vorticity deviation is obtained by subtracting the spatial mean vorticity (denoted by $\langle\cdot\rangle$): $\zeta'(x,y,t) = \zeta(x,y,t) - \langle\zeta\rangle(t)$. The LAVD is then defined as the average of the instantaneous vorticity (ζ') along the flow trajectory (Abernathey & Haller, 2018; Haller et al., 2016):

$$\mathrm{LAVD}_{t_0}^{t_1}(x_0, y_0) = \frac{1}{t_1 - t_0} \int_{t_0}^{t_1} \left| \zeta' \left(X(x_0, y_0, t), Y(x_0, y_0, t), t \right) \right| \mathrm{d}t \tag{9}$$

where X, Y is the position of the particle initially released at point x_0, y_0. Thus, the LAVD is a function of initial position (x_0, y_0) and also the time interval $\left[t_0, t_1\right]$. In Figure 10, the LAVD, integrated for 30 days, is shown for all six experiments. For comparison, we also show the 30-day LAVD fields from a similar region produced from AVISO surface geostrophic velocities in Figure 9 (right panel).

Coherent vortices can be thought of as collectively rotating fluid that is organized into concentric bands around a rotating near-circular core. In our study, this is represented by a family of closed LAVD contours surrounding an innermost LAVD maximum (gray contours in Figure 12). The outer boundary of the rotationally coherent Lagrangian vortex (RCLV) is determined by a threshold on the convexity of the contour (Haller et al., 2016). For this purpose, we utilize the convexity deficiency (CD), as a measure of the convexity of a 2-D LAVD contour. This is the primary tuning parameter of the LAVD method. CD is defined as the difference in area enclosed by the contour and its convex hull divided by the area enclosed by the contour. Once a local maximum of LAVD is detected, we move outward from this maximum across the LAVD contours using a bisection search algorithm until we hit the outermost contour with the target CD. The method does not discriminate between cyclonic or anticyclonic vortices, since absolute values of vorticity are used for the definition.

The procedure is implemented using the `scikit-image` package in Python (van der Walt et al., 2014). The different tuning parameters for this algorithm are CD, the minimum area (in pixels) of the RCLV, and the minimum distance between the center of two RCLVs. Details of the numerical computation and the choice of tuning parameters can be found in Haller et al. (2016), Abernathey and Haller (2018), Tarshish et al. (2018; https://github.com/rabernat/floater). The coherency and population of the identified RCLVs are acutely sensitive to CD, as can be seen in Figure 11.

In Figure 11, we plot the number of RCLVs detected for each choice of CD for all our 2-D particle experiments. For the 2-D cases, we identify RCLVs at long time for the daily and hourly velocities only when we relax the CD to very large values (≥0.05) and set the minimum area and the minimum distance between RCLVS to very small values (≈200 km^2 and ≈50 km, respectively). We observe very convex coherent vortices ($CD < 0.05$) only for weekly averaged velocities. For the hourly and daily averaged velocities, there are no coherent eddies identified at low values of CD.

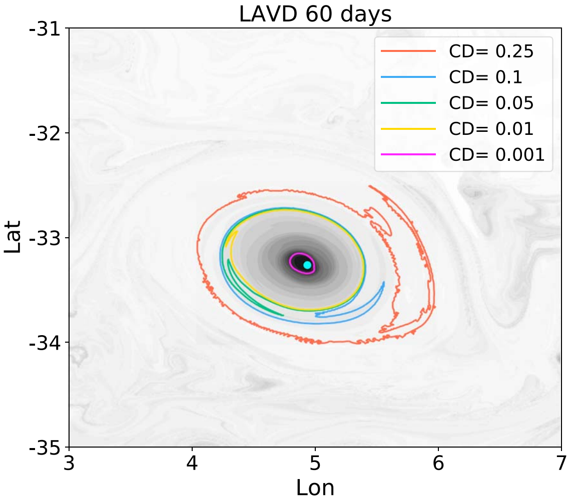

Figure 12. Closed convex contours of Lagrangian averaged vorticity deviation (LAVD) in 2D-w for different choices of convexity deficiency (CD) overlaid on the 60-day LAVD field in gray. The center of the RCLV is marked by a cyan dot.

How does CD affect the character of the identified RCLVs? In Figure 12, we show the outermost LAVD contours for each particular choice of CD for one of the prominent RCLVs detected from the 2D-w case and show the initial and final positions of the particles inside this RCLV for each choice of CD in Figure 13. These two figures show that, if we choose a large CD (0.25), the boundary of the RCLV becomes less defined and exhibits extreme filamentation, and for a low CD (0.001), the permitted RCLV is very small (≈100 km^2). So we settle on 0.1 to be an optimum choice for CD for our study. For this particular choice of CD, with more conservative choices of minimum area (>400 km^2) and minimum distance (>100 km), we only detect about 10–20 RCLVs for the 2D-w and 3D-w cases and none for the rest of the cases. We use the following values of the three parameters for the results shown in the next section: ($CD = 0.1$, minimum area = 400 km^2, and and minimum distance = 100 km). For smaller choices of CD, most of the RCLVs are very small and/or short lived. So while we detect many RCLVs for high values of CD, for the same choice of parameters (minimum distance and minimum area), the algorithm does not detect as many large/long-lived coherent vortices for low CD values, even for the weekly averaged velocities.

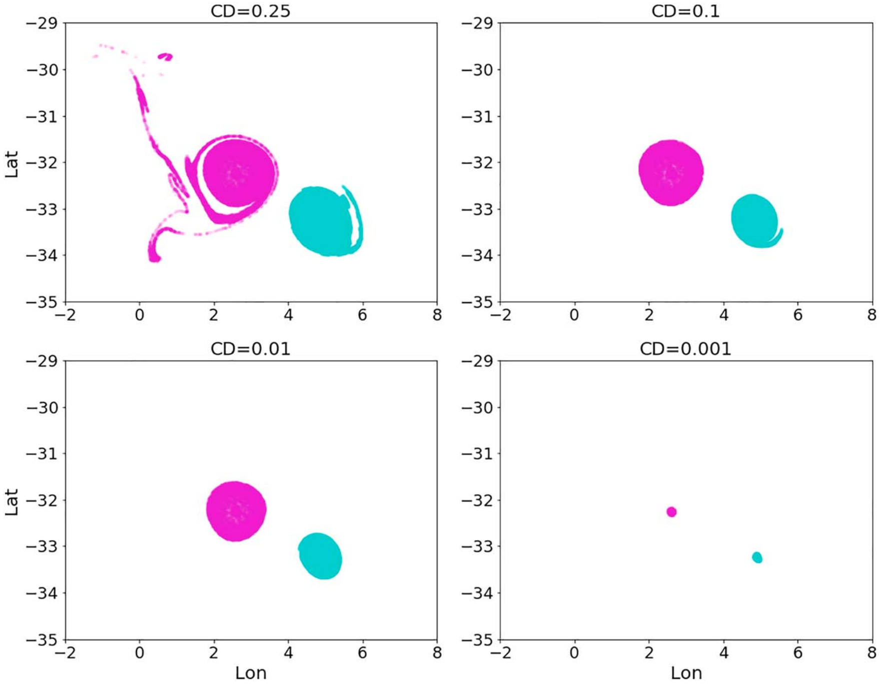

Figure 13. Trajectories of particles over 60 days inside an rotationally coherent Lagrangian vortex (identified from closed convex contours of Lagrangian averaged vorticity deviation in 2D-w) for different choices of convexity deficiency (CD). The cyan circles represent the initial positions of the particles, and the magenta ones are the final positions.

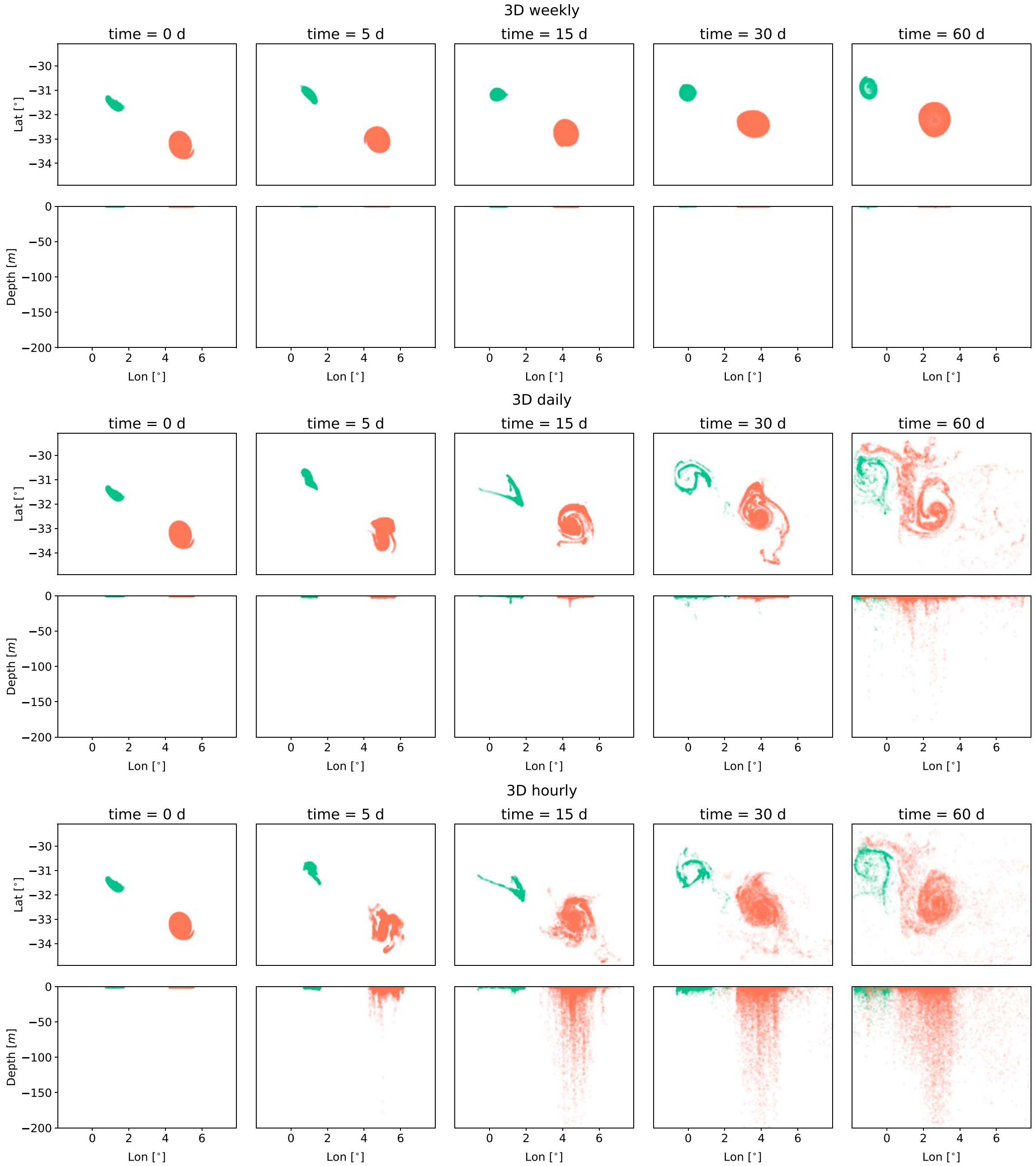

Figure 14. Snapshots at 0, 5, 15, 30, and 60 days showing the evolution of two different rotationally coherent Lagrangian vortices (represented by the red and green dots) detected from closed convex contours ($CD = 0.1$) of LAVD in 3D-w (top), in the horizontal and vertical directions. The middle and bottom two rows show the trajectories of the same particles (with the same initial positions) in 3D-d and 3D-h respectively. (See the supporting information for animations.)

5.3. Case Studies of a Few Coherent Vortices

The analysis above shows that only the weekly averaged velocities produce substantial numbers of RCLVs. In order to determine what causes this breakdown of coherence for daily and hourly velocities, when we travel from 3D-w to 3D-h in Table 1, selecting a few of the relatively large and long-lived RCLVs detected from the 3D-w case and compare the 3-D trajectories of those particles with the same initial positions for the three cases—3D-w, 3D-d, and 3D-h—at different times. Figure 14 shows the evolution of two such RCLVS (represented by the colors, red and green) over 5, 15, 30, and 60 days. The left panels show the initial positions of particles inside two RCLVs detected from closed convex contours ($CD = 0.1$) of LAVD from the 3D-w simulation. The top two rows show the horizontal and vertical positions of the particles inside the RCLV at different times in the 3D-w case. The middle two rows correspond to evolution of those same particles in

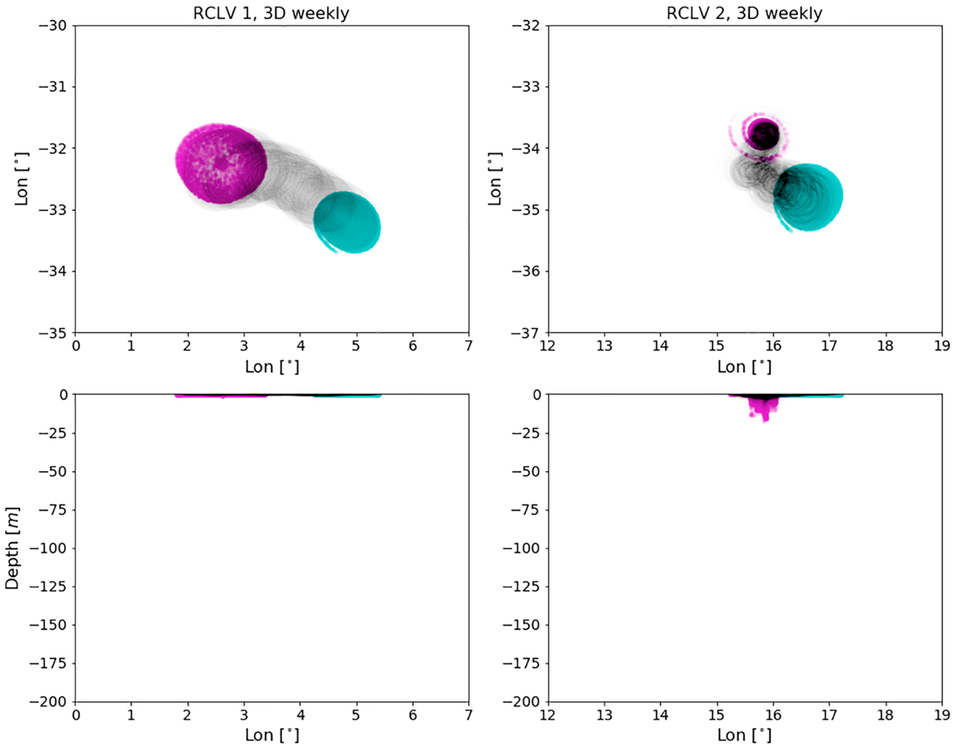

Figure 15. Trajectories of particles inside two different kinds of rotationally coherent Lagrangian vortices (RCLVs) identified from the closed convex contours ($CD = 0.1$) of Lagrangian averaged vorticity deviation in 3D-w experiments: An expanding eddy (left) and a shrinking eddy (right). The cyan dots represent the initial positions, and the magenta dots represent the positions reached by the particles after 60 days. The trajectories for every tenth particle is shown in gray.

the 3D-d case, and the bottom two rows correspond to the 3D-h simulation. In the top panels for each case (horizontal), in the background in gray scale is the backward time FTLE. In the vertical, the trajectory for every tenth particle is shown in gray.

At short times (<15 days), the trajectories from daily velocities show minor filamentation near the vortex edges, but most of the particles stay close to the eddy core. However, at longer times (30 and 60 days), a large number of the particles are scattered horizontally quite far from the eddy core. The scattering of particles is enhanced for the hourly velocity fields. Interestingly, while we see strong filamentary motion with daily velocities, the filaments themselves appear blurry (due to greater scatter by thinner filaments) in the hourly cases. This might be the influence of tides and IGWs, or it could be spurious, due to aliasing of even higher-frequency motions in the hourly velocity snapshots.

Vertical motion is also strongly dependent on filtering. For all the eddies, the particles are contained within the eddy boundary for the 3D-w case, with no or minimal vertical migration. While at short times (<15 days), the 3-D particles stay pretty close to the surface for daily averaged velocities, they exhibit significant vertical motion at long times (>50 days). Vertical motion is the strongest for hourly velocities and the particles are subducted deeper than 200 m in certain regions. Again, we must note that the hourly snapshots used here may introduce spurious vertical particle motion due to aliasing, but we cannot quantify the magnitude of this effect.

After examining a large number of structures, we noticed two main categories of RCLV: expanding and contracting. Such patterns were also observed by Tarshish et al. (2018), and the dynamics driving this motion are the subject of an ongoing study. We show particle trajectories from example RCLVs drawn from each of these two categories in Figure 15 for the 3D-w case. The first kind (RCLV 1, which is the same as the red RCLV in Figure 14) is an expanding eddy. We notice that, for the 3D-w case, the area covered by the eddy at the start of particle advection (represented by the cyan dots) is smaller than the area covered by the eddy at 60 days (magenta dots). This is due to a divergence inside the eddy, presumably associated with upwelling inside

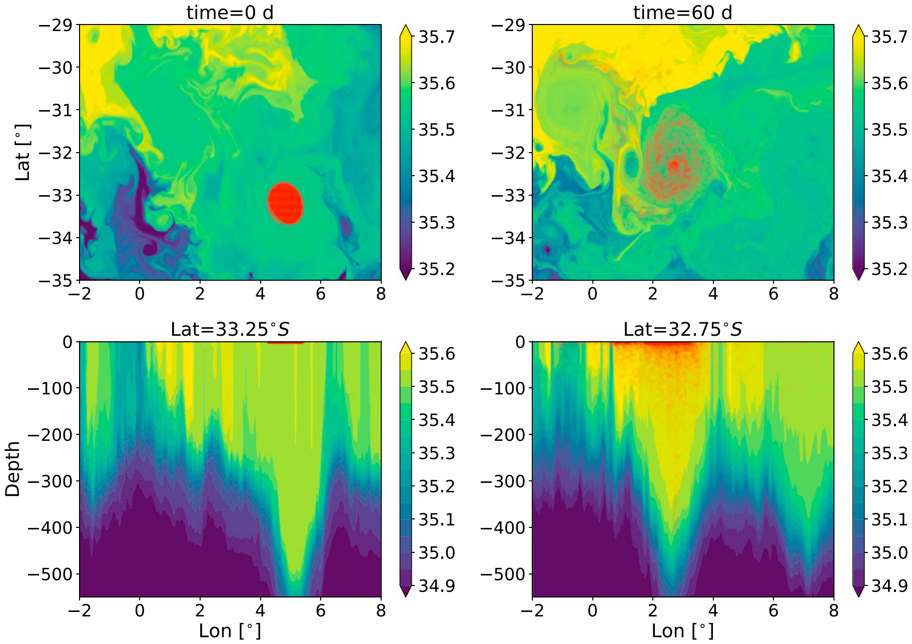

Figure 16. An expanding rotationally coherent Lagrangian vortex (RCLV): Snapshots of the initial (left) and final (right) positions of 3-D particles with the same initial positions as RCLV 1 (left column of Figure 15) advected off-line by hourly velocities superimposed on salinity concentration in the region from online llc4320 simulation output. The colors in the top panels show the salinity at the surface. The bottom panels show a cross section (taken along a latitude line, across the eddy) of the salinity field, and the particles are shown in red. The salinity column marked by the eddy extends to a shallower depth at 60 days, which indicates possible upwelling inside the eddy core. Based on the salinity stratification and the fact that the RCLV expands with time (expansion => upwelling inside), we can reasonably infer that there is possible upwelling inside the eddy core.

the eddy core. However, such upwelling cannot be observed directly in our particle advection experiments, since all the particles were initialized at the surface but is more clearly demonstrated in the salinity field. The second RCLV (right panel, RCLV 2) is a case of a shrinking eddy. Shrinking is likely due to convergence inside the eddy, which can be observed from the pronounced downwelling of the particles at 60 days, even for the weekly velocities. In Figures 16 and 17, the positions of the same particles (cyan dots in Figure 15), advected off-line by the 3-D hourly velocities, are plotted alongside the salinity field (calculated online in the llc4320 simulation) at initial and final times (60 days) .

This scattering of particles away from the eddy core, observed in Figure 14 by unfiltered velocities, is most pronounced for the expanding eddy (RCLV 1; Figure 16) and least pronounced for the contracting eddy (RCLV 2; Figure 17), for which the large-scale divergence counteracts the dispersion.

Figure 17 shows that the downwelling of particles in the shrinking eddy case is associated with increasing salinity anomaly inside the core of the eddy (bottom panels), whereas the expanding eddy corresponding to RCLV 1 in Figure 15 is associated with decreasing salinity anomaly inside the eddy core at depth (bottom right panel Figure 16), likely indicative of net upwelling.

In all these cases, while the eddies do leak particles, the overall eddy signature is still visible as a central cluster of particles. This indicates that, while the overall shape and structure of the eddy inferred from the weekly averaged velocities is persistent, there exist no clear material contour to define the eddy boundary that can be identified by the LAVD technique. Thus, from a Lagrangian point of view, the eddies inferred to be closed and coherent from weekly averaged velocities are generally leaky for velocities with resolved submesoscales and IGWs/tides.

5.4. Vertical Motion

To get a comprehensive view of the vertical motion with the filtered and unfiltered velocities, we examine the depths reached by the 3-D particles at different times. Figure 18 shows a map of particle depths at the end of 30 days for the three velocities for example. The hourly velocity fields transport particles vertically to depths

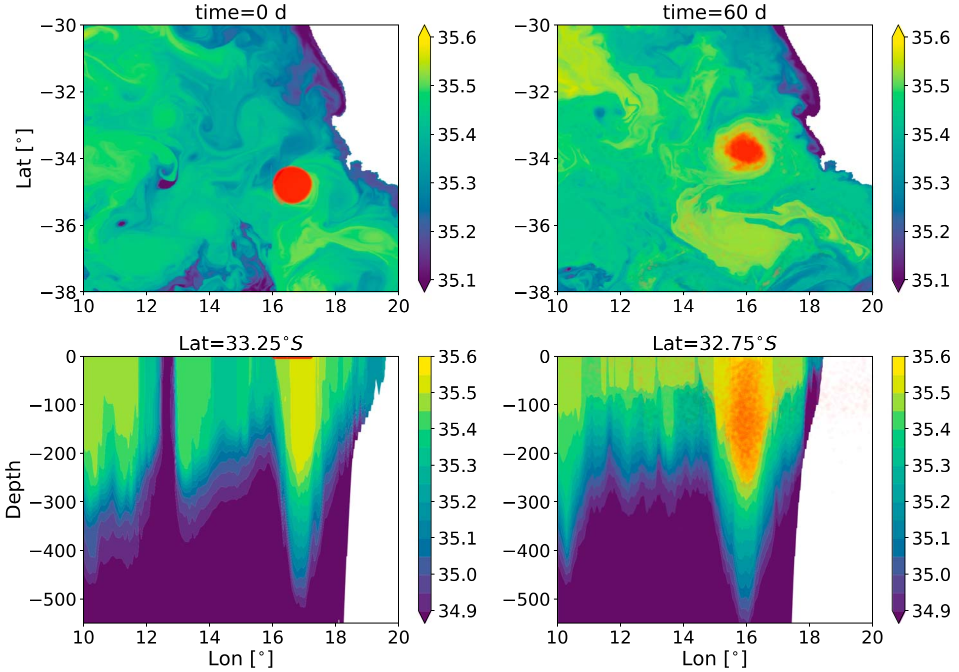

Figure 17. A shrinking rotationally coherent Lagrangian vortex: Snapshots of the initial (left) and final (right) positions of 3-D particles with the same initial positions as rotationally coherent Lagrangian vortex 2 (right column of Figure 15) advected off-line by hourly velocities superimposed on salinity concentration in the region from online llc4320 simulation output. The colors in the top panels show the salinity at the surface. The bottom panels show a cross section (taken along a latitude line, across the eddy) of the salinity field and the particles are shown in red. The salinity at depth inside the eddy is higher at 60 days indicating that there is downwelling inside the eddy core.

of few hundred meters, with the strongest migration being qualitatively collocated with regions of strongest vorticity and KE. This vertical excursion of particles is greatly reduced for the for the lowest temporal resolution (i.e., for the weekly filter), and the particles are surface restricted for the most part. In addition, the distribution of the particle depth at different times (Figure 19) throws some light on the time dependence of vertical migration of particles. For hourly velocities, the particles migrate to a few hundred meters very quickly, and the median depth stays around 120 m for all times, with the number of particles reaching such depths increasing with time. For the daily velocities, a lot of the particles stay near the surface in the beginning (up to 40 days) with enhanced downwelling at later times. The fact that there is reduced vertical motion with the low-pass filtering indicates that there is a strong signature of vertical upwelling/downwelling due to submesoscale/IGWs inside the mesoscale eddies that is lost by temporal filtering. This is also in line with our earlier observation that increasing the level of temporal filtering makes the flow more rotational, filtering out the unbalanced flow asssociated with submesoscale/IGWs, and therefore results in a more 2-D flow.

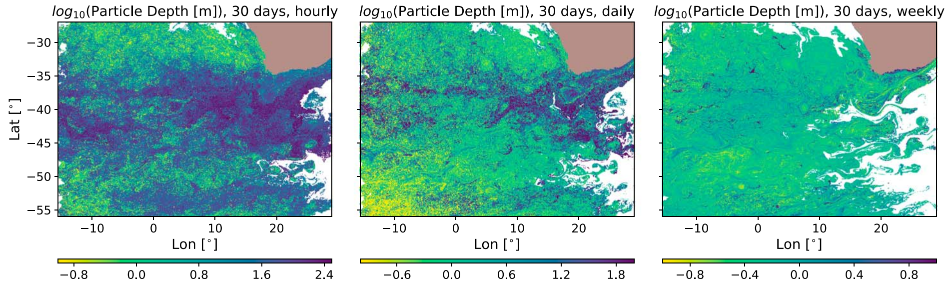

Figure 18. Logarithm ($\log_{10}$) of the depth reached by the particles after 30 days, for (a) hourly velocities, (b) daily averaged velocities, and (c) weekly averaged velocities from the llc4320 numerical model simulations. The white mask represents the initial positions of all particles that reached the edge of the domain at the end of the integration. Land is represented by the brown mask.

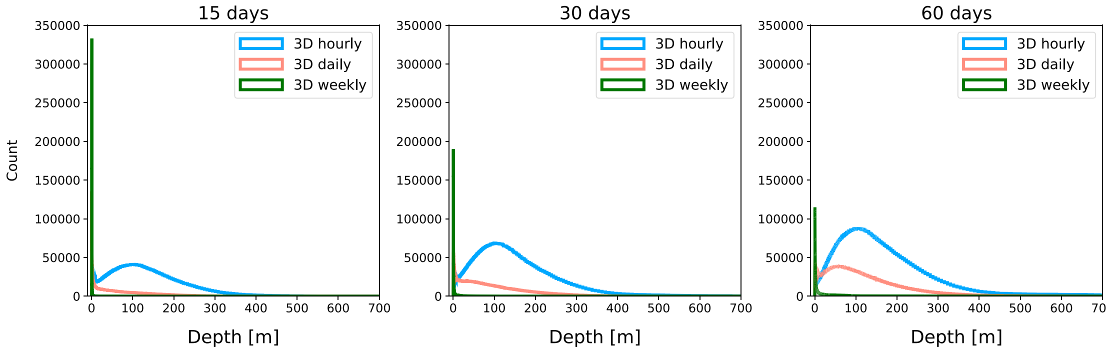

Figure 19. Histogram showing the probability density function of particle depth after 15 days (left), 30 days (middle), and 60 days (right) for all the 3-D particle advection simulations.

Qualitatively, we can assume that the daily filter filters out most of the unbalanced motions associated with tides/IGWs. The presence of deep vertical motions (particles reaching tens to hundreds of meters, cf. Figures 18 and 19) in the daily averaged case (albeit much smaller than that for the hourly velocities), collocated with regions of high vorticity (Figure 10) indicates that unbalanced submesoscale eddies induce significant vertical motion in addition to IGWs/tides. However, in our present framework, it is difficult to quantitatively assess what proportion of the vertical motion is due to IGWs/tides compared to unbalanced submesoscale eddies.

6. Discussion and Conclusions

In this study, we studied the Lagrangian transport properties associated with model velocities from a very high resolution ((1/48)° horizontal) numerical model (MITgcm) simulation (llc4320) with nonlocally forced tides in a part of the South Atlantic Ocean, covering the Agulhas retroflection and part of the ACC. Our primary aim was to identify the influence of fast–time scale motions on Lagrangian transport in this new type of ocean model.

The power spectral density in frequency space of the surface KE from the hourly model output velocity fields revealed the presence of strong IGWs and tides in the domain. We time averaged this hourly output over daily and weekly time scales to generate two additional velocity records. The wavenumber power spectrum corresponding to the three velocity fields (hourly unfiltered, daily filtered, and weekly filtered) showed that time averaging predominantly acts to remove energy from smaller length scales. A Helmholtz decomposition of the 1-D wavenumber spectrum (Bühler et al., 2014; Rocha, Chereskin, et al., 2016) into horizontally nondivergent and divergent components revealed that temporal filtering removes unbalanced divergent motions more effectively than the balanced geostrophic motions. Although we did not explicitly perform an observing system simulation experiment, we noted that, among our different experiments, the weekly filtered velocities represent the closest approximation to velocities inferred from satellite altimetry.

We then used the three sets of velocity fields to advect particles at the surface using only the horizontal components of the velocity field (2-D particles) and in full depth using all three components of the velocity field (3-D particles). Using these Lagrangian trajectories, we computed some bulk transport statistics, relative dispersion, and diffusivity and also measures of kinematic coherence, FTLE and LAVD.

Relative dispersion and relative diffusivity calculations showed that the high-frequency motions play a significant role in lateral transport, particularly at small scales. Temporal filtering reduced the effectiveness of turbulent diffusion at smaller scales and faster times, with the reduction in diffusion being greater for the weekly filter than the daily filter. The diffusivity at the largest scales was also reduced, but this impact was smaller than the reduction at the smaller scale. For the Agulhas region, the difference between the diffusivities from unfiltered and filtered velocities at small scales was greater than that for the ACC region. This might be caused by the ACC having a less energetic submesoscale velocity field than the Agulhas region, which can also be seen in the KE spectrum. A weaker submesoscale field might be a result of the model resolution being inadequate in the ACC, where the deformation radius is smaller, or because of the mean flow suppressing the growth of submesoscale instabilities (Taylor et al., 2018).

Our coherent structure diagnostics generally showed that Lagrangian coherence was degraded when using the unfiltered and daily velocities, compared to the weekly averaged velocities. FTLE fields appeared noisy for hourly velocities at long times, and we did not observe the characteristic large-scale, well-defined FTLE ridges that are typically seen in studies with altimetry-derived velocities (Beron-Vera et al., 2008) even with daily averaged velocities, as the large-scale transport barriers got drowned in the intricate submesoscale structures. Weekly averaged velocity fields produced more coherent material transport barriers in the FTLE field.

Using the LAVD method of Haller et al. (2016), we identified RCLVs over a range of CD parameters for the raw and filtered velocities. We found that large-scale coherent RCLVs are only readily identifiable in weekly averaged velocities. While we found RCLVs with daily filtered velocities, they were very small and short lived. With hourly velocites, we only found RCLVs with unreasonably large CD values. We examined the trajectories in the vicinity of the RCLVs identified from the weekly data to further understand how high-frequency flows caused material coherence to break down. At daily resolution, strong filaments appeared around the boundaries of the eddies. At hourly resolution, these filaments blurred into broader patches.

Perhaps, the most important and controversial finding of our study relates to the nature of coherent mesoscale eddies (Agulhas rings specifically). A major question for mesoscale oceanography is *what fraction of the overall turbulent transport of tracers arises from trapping and translation of fluid within coherent eddies*. Some studies using Eulerian eddy tracking methods (e.g., Dong et al., 2014) have estimated this fraction to be quite high. Recently, objective Lagrangian methods, driven by AVISO-derived velocities, have been applied to this question in different regions of the ocean (Abernathey & Haller, 2018; Wang et al., 2016), largely concluding that Eulerian eddy tracking approaches overestimate the coherent transport. However, despite the precision and objectivity of the Lagrangian approach, these estimates are only as reliable as the velocities used to generate the trajectories. Do submesoscale flows, tides, and IGWs substantially alter mesoscale LCS?

To date, the most comprehensive studies of this question can be found in a recent pair of papers focused on a single eddy in the Gulf of Mexico. Beron-Vera, Olascoaga, et al. (2018) identified this eddy using the objective geodesic method (Haller & Beron-Vera, 2013; Wang et al., 2015) applied to AVISO-derived velocities. They argued that evidence from other observations, particularly drogued surface drifters and remotely sensed ocean color, confirmed the coherent, material nature of the identified eddy boundary and was consistent with the ~200-day lifetime. However, the same geodesic method applied to velocities from a submesoscale-permitting, data-assimilating simulation at 1-km resolution failed to identify any coherent structure, despite the fact that relative dispersion statistics from the simulated trajectories agreed well with drifter statistics. The authors speculated that this failure could be an artifact of the data assimilation process, related to more general challenges of ocean data assimilation in the submesoscale regime (Sandery & Sakov, 2017). Studying the same eddy, however, Beron-Vera, Hadjighasem, et al. (2018) reached a slightly different conclusion: While the geodesic eddy method was too strict to find any Lagrangian coherent structure, the LAVD method was more successful. With a high enough choice of CD, mesoscale eddies were shown to persist, even though their boundaries exhibited increased filamentation relative to the extremely coherent boundaries inferred from satellite altimetry. Haza et al. (2016), on the other hand, showed that mesoscale transport barriers obtained from altimeter observation simulating velocity fields were extremely leaky and in some cases leaked almost 50% of the tracers in the presence of submesoscale motions using a high-resolution regional simulation (HYCOM). Taken together, these studies give a mixed assessment of the role of the submesoscale: Is the difficulty of finding coherent mesoscale eddies in submesoscale-permitting simulations a problem with the model or with the method? More broadly, how general are the conclusions that can be drawn from the study of a single eddy?

Our experiments avoid the confounding effects of data assimilation and examine a much broader spatial area. The submesoscale (Rocha, Chereskin, et al., 2016; Rocha, Gille, et al., 2016) and IGW/tidal variability (Savage et al., 2017) in the llc simulation agrees reasonably well with in situ observations in the wavenumber and frequency domain, showing that the amplitude of these motions is physically plausible. We find that the Agulhas rings detected from weekly averaged velocities are much more coherent than the “true” Agulhas rings, as represented by the daily or hourly velocities. The high-frequency motions cause material to leak substantially across the eddy boundaries identified from the weekly averaged flow. While visual examination of the trajectories shows there appears to be a Lagrangian core to the eddies, material boundaries are not readily identifiable using the LAVD approach. Most LCS identification methods have been validated using two-dimensional turbulence as a test case (Hadjighasem et al., 2017), which is arguably dynamically similar to the weekly averaged flow. Our study thus suggests that new approaches to identifying materially coherent eddies may be needed in the regime represented by the llc simulation.

We attribute this breakdown of observed coherence at high temporal resolutions to the submesoscale and IGW/tidal signature in high-frequency data. The absence of small-scale motions associated with the IGW and submesoscale currents, in low temporal resolution data, may lead to overestimating Lagrangian coherence in satellite altimetry-derived fields. As such we should exercise caution and account for these biases when make transport estimates from high-spatial-resolution but temporally sparse satellite altimetry-derived geostrophic velocities. The present results therefore have implications for high-resolution altimeters, for example, the upcoming SWOT mission. As in current altimeter technology, swath altimetry (SWOT) will likely alias high-frequency motions. Further, unbalanced flows may upset the estimation of O(10-km) resolution surface geostrophic velocities. That is, the high-wavenumber SSH variability may represent a different, ageostrophic, physical regime, where geostrophy might not be the best route to infer velocities. Tidal and supertidal motions, aliased by satellite altimetry, will need to be properly understood if we are to gain meaningful insight regarding the dynamics of both high- and low-frequency motions at small scales from this upcoming mission. These are some of the problems that merit further investigation.

Acknowledgments

Balwada and Abernathey acknowledge support from NASA award NNX16AJ35G. Abernathey and Sinha acknowledge additional support from NSF award OCE 1553593. Tarshish acknowledges support from the U.S. Department of Energy under award DE-SC0012457. Some of the relevant analysis code used for calculating the LCS diagnostics and power spectra can be found in the repository (https://github.com/anirban89/llc_lcs_JAMES.git). The code used to compile MITgcm can be found in https://github.com/anirban89/code_lavd_nonnormal.git, and the datafiles (for our off-line model experiments) in the GitHub website (https://github.com/anirban89/llc_data_files.git). The input files, which were generated from llc4320 output (code available in above mentioned repository), are too large to put in a repository and can be made available upon request.

References

Abernathey, R., & Ferreira, D. (2015). Southern ocean isopycnal mixing and ventilation changes driven by winds. *Geophysical Research Letters*, *42*, 10,357–10,365. https://doi.org/10.1002/2015GL066238

Abernathey, R., & Haller, G. (2018). Transport by Lagrangian vortices in the eastern Pacific. *Journal of Physical Oceanography*, *48*(3), 667–685. https://doi.org/10.1175/JPO-D-17-0102.1

Abernathey, R. P., & Marshall, J (2013). Global surface eddy diffusivities derived from satellite altimetry. *Journal of Geophysical Research: Oceans*, *118*, 901–916. https://doi.org/10.1002/jgrc.20066

Abraham, E. R., & Bowen, M. M. (2002). Chaotic stirring by a mesoscale surface-ocean flow. *Chaos: An Interdisciplinary Journal of Nonlinear Science*, *12*(2), 373–381. https://doi.org/10.1063/1.1481615

Alford, M. H., MacKinnon, J. A., Simmons, H. L., & Nash, J. D. (2016). Near-inertial internal gravity waves in the ocean. *Annual Review of Marine Science*, *8*, 95–123. https://doi.org/10.1146/annurev-marine-010814-015746

Aluie, H., Hecht, M., & Vallis, G. K. (2018). Mapping the energy cascade in the North Atlantic Ocean: The coarse-graining approach. *Journal of Physical Oceanography*, *48*(2), 225–244. https://doi.org/10.1175/JPO-D-17-0100.1

Babiano, A., Basdevant, C., Le Roy, P., & Sadourny, R. (1990). Relative dispersion in two-dimensional turbulence. *Journal of Fluid Mechanics*, *214*, 535–557. https://doi.org/10.1017/S0022112090000258

Balwada, D., LaCasce, J. H., & Speer, K. G. (2016). Scale-dependent distribution of kinetic energy from surface drifters in the Gulf of Mexico. *Geophysical Research Letters*, *43*, 10,856–10,863. https://doi.org/10.1002/2016GL069405

Balwada, D., Smith, K. S., & Abernathey, R. (2018). Submesoscale vertical velocities enhance tracer subduction in an idealized Antarctic Circumpolar Current. *Geophysical Research Letters*, *45*, 9790–9802. https://doi.org/10.1029/2018GL079244

Balwada, D., Speer, K. G., LaCasce, J. H., Owens, W. B., Marshall, J., & Ferrari, R. (2016). Circulation and stirring in the Southeast Pacific Ocean and the Scotia Sea sectors of the Antarctic Circumpolar Current. *Journal of Physical Oceanography*, *46*(7), 2005–2027. https://doi.org/10.1175/JPO-D-15-0207.1

Barkan, R., Winters, K. B., & McWilliams, J. C. (2017). Stimulated imbalance and the enhancement of eddy kinetic energy dissipation by internal waves. *Journal of Physical Oceanography*, *47*(1), 181–198. https://doi.org/10.1175/JPO-D-16-0117.1

Bennett, A. F. (1984). Relative dispersion: Local and nonlocal dynamics. *Journal of the Atmospheric Sciences*, *41*(11), 1881–1886. https://doi.org/10.1175/1520-0469(1984)041<1881:RDLAND>2.0.CO;2

Beron-Vera, F. J. (2010). Mixing by low- and high-resolution surface geostrophic currents. *Journal of Geophysical Research*, *115*, C10027. https://doi.org/10.1029/2009JC006006

Beron-Vera, F. J., Hadjighasem, A., Xia, O., Olascoaga, M. J., & Haller, G. (2018). Coherent Lagrangian swirls among submesoscale motions. *Proceedings of the National Academy of Sciences*. https://doi.org/10.1073/pnas.1701392115

Beron-Vera, F., Olascoaga, M., & Goni, G. (2008). Oceanic mesoscale eddies as revealed by Lagrangian coherent structures. *Geophysical Research Letters*, *35*, L12603. https://doi.org/10.1029/2008GL033957

Beron-Vera, F. J., Olascoaga, M. J., Wang, Y., Triñanes, J., & Pérez-Brunius, P. (2018). Enduring Lagrangian coherence of a Loop Current ring assessed using independent observations. *Scientific Reports*, *8*(1), 11,275–11,275. https://doi.org/10.1038/s41598-018-29582-5

Beron-Vera, F. J., Wang, Y., Olascoaga, M. J., Goni, G. J., & Haller, G. (2013). Objective detection of oceanic eddies and the Agulhas leakage. *Journal of Physical Oceanography*, *43*(7), 1426–1438. https://doi.org/10.1175/JPO-D-12-0171.1

Boccaletti, G., Ferrari, R., & Fox-Kemper, B. (2007). Mixed layer instabilities and restratification. *Journal of Physical Oceanography*, *37*(9), 2228–2250. https://doi.org/10.1175/JPO3101.1

Bühler, O., Callies, J., & Ferrari, R. (2014). Wave–vortex decomposition of one-dimensional ship-track data. *Journal of Fluid Mechanics*, *756*, 1007–1026. https://doi.org/10.1017/jfm.2014.488

Callies, J., & Ferrari, R. (2013). Interpreting energy and tracer spectra of upper-ocean turbulence in the submesoscale range (1–200 km). *Journal of Physical Oceanography*, *43*(11), 2456–2474. https://doi.org/10.1175/JPO-D-13-063.1

Callies, J., Ferrari, R., & Bühler, O. (2014). Transition from geostrophic turbulence to inertia-gravity waves in the atmospheric energy spectrum. *Proceedings of the National Academy of Sciences*, *111*(48), 17,033–17,038. https://doi.org/10.1073/pnas.1410772111

Capet, X., McWilliams, J. C., Molemaker, M. J., & Shchepetkin, A. F. (2008). Mesoscale to submesoscale transition in the california current system. Part I: Flow structure, eddy flux, and observational tests. *Journal of Physical Oceanography*, *38*(1), 29–43. https://doi.org/10.1175/2007JPO3671.1

Charney, J. G. (1971). Geostrophic turbulence. *Journal of the Atmospheric Sciences*, *28*(6), 1087–1095. https://doi.org/10.1175/1520-0469(1971)028<1087:GT>2.0.CO;2

Chelton, D. B., Schlax, M. G., Samelson, R. M., & de Szoeke, R. A. (2007). Global observations of large oceanic eddies. *Geophysical Research Letters*, *34*, L15606. https://doi.org/10.1029/2007GL030812

Choi, J., Bracco, A., Barkan, R., Shchepetkin, A. F., McWilliams, J. C., & Molemaker, J. M. (2017). Submesoscale dynamics in the Northern Gulf of Mexico. Part III: Lagrangian implications. *Journal of Physical Oceanography*, *47*(9), 2361–2376. https://doi.org/10.1175/JPO-D-17-0036.1

D'Asaro, E., Lee, C., Rainville, L., Harcourt, R., & Thomas, L. (2011). Enhanced turbulence and energy dissipation at ocean fronts. *Science*, *332*(6027), 318–322. https://doi.org/10.1126/science.1201515

d'Ovidio, F., Isern-Fontanet, J., Lopez, C., Hernandez-Garcia, E., & Garcia-Ladona, E. (2009). Comparison between Eulerian diagnostics and finite-size Lyapunov exponents computed from altimetry in the Algerian basin. *Deep Sea Research Part I: Oceanographic Research Papers*, *56*(1), 15–31. https://doi.org/10.1016/j.dsr.2008.07.014

Davis, R. E. (1985). Drifter observations of coastal surface currents during code: The statistical and dynamical views. *Journal of Geophysical Research*, *90*(C3), 4756–4772. https://doi.org/10.1029/JC090iC03p04756

Davis, R. E. (1991). Observing the general circulation with floats. *Deep Sea Research Part A. Oceanographic Research Papers*, *38*, S531–S571. https://doi.org/10.1016/S0198-0149(12)

Dong, C., McWilliams, J. C., Liu, Y., & Chen, D. (2014). Global heat and salt transports by eddy movement. *Nature Communications*, *5*, 3294. https://doi.org/10.1038/ncomms4294

Ducet, N., Le Traon, P. Y., & Reverdin, G. (2000). Global high-resolution mapping of ocean circulation from Topex/Poseidon and ERS-1 and -2. *Journal of Geophysical Research*, *105*(C8), 19,477–19,498. https://doi.org/10.1029/2000JC900063

Elipot, S., Lumpkin, R., Perez, R. C., Lilly, J. M., Early, J. J., & Sykulski, A. M. (2016). A global surface drifter data set at hourly resolution. *Journal of Geophysical Research: Oceans*, *121*, 2937–2966. https://doi.org/10.1002/2016JC011716

Faghmous, J. H., Frenger, I., Yao, Y., Warmka, R., Lindell, A., & Kumar, V. (2015). A daily global mesoscale ocean eddy dataset from satellite altimetry. *Scientific Data*, *2*, 150,028–150,028. https://doi.org/10.1038/sdata.2015.28

Farazmand, M., & Haller, G. (2012). Computing Lagrangian coherent structures from their variational theory. *Chaos: An Interdisciplinary Journal of Nonlinear Science*, *22*(1), 013128. https://doi.org/10.1063/1.3690153

Ferrari, R., & Wunsch, C. (2009). Ocean circulation kinetic energy: Reservoirs, sources, and sinks. *Annual Review of Fluid Mechanics*, *41*, 253–282. https://doi.org/10.1146/annurev.fluid.40.111406.102139

Fjortoft, R., Gaudin, J.-M., Pourthié, N., Lalaurie, J.-C., Mallet, A., Nouvel, J.-F., et al. (2014). KaRin on SWOT: Characteristics of near-nadir Ka-band interferometric SAR imagery. *IEEE Transactions on Geoscience and Remote Sensing*, *52*, 2172–2185. https://doi.org/10.1109/TGRS.2013.2258402

Foussard, A., Berti, S., Perrot, X., & Lapeyre, G. (2017). Relative dispersion in generalized two-dimensional turbulence. *Journal of Fluid Mechanics*, *821*, 358–383. https://doi.org/10.1017/jfm.2017.253

Fox-Kemper, B., Ferrari, R., & Hallberg, R. (2008). Parameterization of mixed layer eddies. Part I: Theory and diagnosis. *Journal of Physical Oceanography*, *38*(6), 1145–1165. https://doi.org/10.1175/2007JPO3792.1

Fu, L.-L., Chelton, D. B., Traon, P.-Y. L., & Morrow, R. (2010). Eddy dynamics from satellite altimetry. *Oceanography*, *23*, 14–25. https://doi.org/10.5670/oceanog.2010.02

Fu, L. L., & Ferrari, R. (2008). Observing mesoscale to submesoscale dynamics today, and in the future with SWOT. *EOS*, *89*, 2689–2691. https://doi.org/10.1109/IGARSS.2011.6049757

Gent, P. R., & Mcwilliams, J. C. (1990). Isopycnal mixing in ocean circulation models. *Journal of Physical Oceanography*, *20*(1), 150–155. https://doi.org/10.1175/1520-0485(1990)020<0150:IMIOCM>2.0.CO;2

Gent, P. R., Willebrand, J., McDougall, T. J., & McWilliams, J. C. (1995). Parameterizing eddy-induced tracer transports in ocean circulation models. *Journal of Physical Oceanography*, *25*(4), 463–474. https://doi.org/10.1175/1520-0485(1995)025<0463:PEITTI>2.0.CO;2

Gnanadesikan, A., Russell, A., Pradal, M.-A., & Abernathey, R. (2017). Impact of lateral mixing in the ocean on El Niño in a suite of fully coupled climate models. *Journal of Advances in Modeling Earth Systems*, *9*, 2493–2513. https://doi.org/10.1002/2017MS000917

Griffa, A., Piterbarg, L. I., & Özgökmen, T. (2004). Predictability of Lagrangian particle trajectories: Effects of smoothing of the underlying Eulerian flow. *Journal of Marine Research*, *62*(1), 1–35. https://doi.org/10.1357/00222400460744609

Groeskamp, S., Abernathey, R. P., & Klocker, A. (2018). Water mass transformation by cabbeling and thermobaricity. *Geophysical Research Letters*, *43*, 10,835–10,845. https://doi.org/10.1002/2016GL070860

Groeskamp, S., Sloyan, B. M., Zika, J. D., & McDougall, T. J. (2017). Mixing inferred from an ocean climatology and surface fluxes. *Journal of Physical Oceanography*, *47*(3), 667–687. https://doi.org/10.1175/JPO-D-16-0125.1

Grooms, I., & Zanna, L. (2017). A note on "Toward a stochastic parameterization of ocean mesoscale eddies". *Ocean Modelling*, *113*, 30–33. https://doi.org/10.1016/j.ocemod.2017.03.007

Hadjighasem, A., Farazmand, M., Blazevski, D., Froyland, G., & Haller, G. (2017). A critical comparison of Lagrangian methods for coherent structure detection. *Chaos: An Interdisciplinary Journal of Nonlinear Science*, *27*(5), 053104. https://doi.org/10.1063/1.4982720

Haller, G. (2002). Lagrangian coherent structures from approximate velocity data. *Physics of Fluids*, *14*(6), 1851–1861. https://doi.org/10.1063/1.1477449

Haller, G. (2011). A variational theory of hyperbolic Lagrangian coherent structures. *Physica D: Nonlinear Phenomena*, *240*(7), 574–598. https://doi.org/10.1016/j.physd.2010.11.010

Haller, G. (2015). Lagrangian coherent structures. *Annual Review of Fluid Mechanics*, *47*, 137–162. https://doi.org/10.1146/annurev-fluid-010313-141322

Haller, G., & Beron-Vera, F. (2013). Coherent Lagrangian vortices: The black holes of turbulence. *Journal of Fluid Mechanics*, *731*, R4. https://doi.org/10.1017/jfm.2013.391

Haller, G., Hadjighasem, A., Farazmand, M., & Huhn, F. (2016). Defining coherent vortices objectively from the vorticity. *Journal of Fluid Mechanics*, *795*, 136–173. https://doi.org/10.1017/jfm.2016.151

Haller, G., & Sapsis, T. (2011). Lagrangian coherent structures and the smallest finite-time Lyapunov exponent. *Chaos: An Interdisciplinary Journal of Nonlinear Science*, *21*(2), 023115. https://doi.org/10.1063/1.3579597

Haller, G., & Yuan, G. (2000). Lagrangian coherent structures and mixing in two-dimensional turbulence. *Physica D: Nonlinear Phenomena*, *147*(3), 352–370. https://doi.org/10.1016/S0167-2789(00)00142-1

Haza, A., Özgökmen, T., & Hogan, P. (2016). Impact of submesoscales on surface material distribution in a Gulf of Mexico mesoscale eddy. *Ocean Modelling*, *107*, 28–47. https://doi.org/10.1016/j.ocemod.2016.10.002

Holloway, G. (1986). Estimation of oceanic eddy transports from satellite altimetry. *Nature*, *323*, 243–244. https://doi.org/10.1038/323243a0

Isern-Fontanet, J., Garcia-Ladona, E., & Font, J. (2003). Identification of marine eddies from altimetric maps. *Journal of Atmospheric and Oceanic Technology*, *20*(5), 772–778. https://doi.org/10.1175/1520-0426(2003)20<772:IOMEFA>2.0.CO;2

Isern-Fontanet, J., Garcia-Ladona, E., & Font, J. (2006). Vortices of the mediterranean sea: An altimetric perspective. *Journal of Physical Oceanography*, *36*(1), 87–103. https://doi.org/10.1175/JPO2826.1

Keating, S. R., Majda, A. J., & Smith, K. S. (2012). New methods for estimating ocean eddy heat transport using satellite altimetry. *Monthly Weather Review*, *140*(5), 1703–1722. https://doi.org/10.1175/MWR-D-11-00145.1

Keating, S. R., Smith, K. S., & Kramer, P. R. (2011). Diagnosing lateral mixing in the upper ocean with virtual tracers: Spatial and temporal resolution dependence. *Journal of Physical Oceanography*, *41*(8), 1512–1534. https://doi.org/10.1175/2011JPO4580.1

Khatiwala, S., Tanhua, T., Mikaloff Fletcher, S., Gerber, M., Doney, S. C., Graven, H. D., et al. (2013). Global ocean storage of anthropogenic carbon. *Biogeosciences*, *10*(4), 2169–2191. https://doi.org/10/2169/2013

Klein, P., Hua, B. L., Lapeyre, G., Capet, X., Le Gentil, S., & Sasaki, H. (2008). Upper ocean turbulence from high-resolution 3D simulations. *Journal of Physical Oceanography*, *38*(8), 1748–1763. https://doi.org/10.1175/2007JPO3773.1

Klein, P., & Lapeyre, G. (2009). The oceanic vertical pump induced by mesoscale and submesoscale turbulence. *Annual Review of Marine Science*, *1*, 351–375. https://doi.org/10.1146/annurev.marine.010908.163704

Klocker, A., & Abernathey, R. (2014). Global patterns of mesoscale eddy properties and diffusivities. *Journal of Physical Oceanography*, *44*(3), 1030–1046. https://doi.org/10.1175/JPO-D-13-0159.1

LaCasce, J. (2008). Statistics from Lagrangian observations. *Progress in Oceanography*, *77*(1), 1–29. https://doi.org/10.1016/j.pocean.2008.02.002

LaCasce, J. H., Ferrari, R., Marshall, J., Tulloch, R., Balwada, D., & Speer, K. (2014). Float-derived isopycnal diffusivities in the DIMES experiment. *Journal of Physical Oceanography*, *44*(2), 764–780. https://doi.org/10.1175/JPO-D-13-0175.1

Lapeyre, G., & Klein, P. (2006). Dynamics of the upper oceanic layers in terms of surface quasigeostrophy theory. *Journal of Physical Oceanography*, *36*(2), 165–176. https://doi.org/10.1175/JPO2840.1

Large, W. G., & Yeager, S. (2004). Diurnal to decadal global forcing for ocean and sea-ice models: The data sets and flux climatologies (Tech. rep.) Boulder: NCAR/UCAR. https://doi.org/10.5065/D6KK98Q6

Le Traon, P. Y., Klein, P., Hua, B. L., & Dibarboure, G. (2008). Do altimeter wavenumber spectra agree with the interior or surface quasigeostrophic theory? *Journal of Physical Oceanography*, *38*(5), 1137–1142. https://doi.org/10.1175/2007JPO3806.1

Liang, X., Piecuch, C. G., Ponte, R. M., Forget, G., Wunsch, C., & Heimbach, P. (2017). Change of the global ocean vertical heat transport over 1993–2010. *Journal of Climate*, *30*(14), 5319–5327. https://doi.org/10.1175/JCLI-D-16-0569.1

Lumpkin, R., & Johnson, G. C. (2013). Global ocean surface velocities from drifters: Mean, variance, El Niño–Southern Oscillation response, and seasonal cycle. *Journal of Geophysical Research: Oceans*, *118*, 2992–3006. https://doi.org/10.1002/jgrc.20210

Mahadevan, A. (2016). The impact of submesoscale physics on primary productivity of plankton. *Annual Review of Marine Science*, *8*(1), 161–184. https://doi.org/10.1146/annurev-marine-010814-015912

Mahadevan, A., & Campbell, J. W. (2002). Biogeochemical patchiness at the sea surface. *Geophysical Research Letters*, *29*(19), 1926. https://doi.org/10.1029/2001GL014116

Mariano, A., Kourafalou, V., Srinivasan, A., Kang, H., Halliwell, G., Ryan, E., & Roffer, M. (2011). On the modeling of the 2010 Gulf of Mexico oil spill. *Dynamics of Atmospheres and Oceans*, *52*(1-2), 322–340.

Marshall, J., Scott, J. R., Romanou, A., Kelley, M., & Leboissetier, A. (2017). The dependence of the ocean's MOC on mesoscale eddy diffusivities: A model study. *Ocean Modelling*, *111*, 1–8. https://doi.org/10.1016/j.ocemod.2017.01.001

Marshall, J., Shuckburgh, E., Jones, H., & Hill, C. (2006). Estimates and implications of surface eddy diffusivity in the southern ocean derived from tracer transport. *Journal of Physical Oceanography*, *36*(9), 1806–1821. https://doi.org/10.1175/JPO2949.1

Martin, A. P. (2003). Phytoplankton patchiness: The role of lateral stirring and mixing. *Progress in Oceanography*, *57*(2), 125–174. https://doi.org/10.1016/S0079-6611(03)00085-5

Maxey, M. R., & Riley, J. J. (1983). Equation of motion for a small rigid sphere in a nonuniform flow. *The Physics of Fluids*, *26*(4), 883–889. https://doi.org/10.1063/1.864230

McWilliams, J. C. (2016). Submesoscale currents in the ocean. *Proceedings of the Royal Society A: Mathematical, Physical and Engineering Sciences*, *472*(2189), 20160117. https://doi.org/10.1098/rspa.2016.0117

Morrow, R., Birol, F., Griffin, D., & Sudre, J. (2004). Divergent pathways of cyclonic and anticyclonic ocean eddies. *Geophysical Research Letters*, *31*, L24311. https://doi.org/10.1029/2004GL020974

Munk, W. (1981). Internal waves and small-scale processes. In B. A. Warren & C. Wunsch (Eds.), *Evolution of physical oceanography: Scientific surveys in honor of henry stommel* (pp. 264–291). Cambridge: MIT Press.

Okubo, A. (1971). Oceanic diffusion diagrams. *Deep Sea Research and Oceanographic Abstracts*, *18*(8), 789–802. https://doi.org/10.1016/0011-7471(71)90046-5

Omand, M. M., D'Asaro, E. A., Lee, C. M., Perry, M. J., Briggs, N., Cetinić, I., & Mahadevan, A. (2015). Eddy-driven subduction exports particulate organic carbon from the spring bloom. *Science*, *348*(6231), 222–225. https://doi.org/10.1126/science.1260062

Pierrehumbert, R. T., & Yang, H. (1993). Global chaotic mixing on isentropic surfaces. *Journal of the Atmospheric Sciences*, *50*(15), 2462–2480. https://doi.org/10.1175/1520-0469(1993)050<2462:GCMOIS>2.0.CO;2

Poje, A. C., Haza, A. C., Özgökmen, T. M., Magaldi, M. G., & Garraffo, Z. D. (2010). Resolution dependent relative dispersion statistics in a hierarchy of ocean models. *Ocean Modelling*, *31*(1-2), 36–50. https://doi.org/10.1016/j.ocemod.2009.09.002

Poje, A. C., Özgökmen, T. M., Lipphardt, B. L., Haus, B. K., Ryan, E. H., Haza, A. C., et al. (2014). Submesoscale dispersion in the vicinity of the Deepwater Horizon spill. *Proceedings of the National Academy of Sciences*, *111*(35), 12,693–12,698. https://doi.org/10.1073/pnas.1402452111

Qiu, B., Chen, S., Klein, P., Ubelmann, C., Fu, L.-L., & Sasaki, H. (2016). Reconstructability of three-dimensional upper-ocean circulation from SWOT sea surface height measurements. *Journal of Physical Oceanography*, *46*(3), 947–963. https://doi.org/10.1175/JPO-D-15-0188.1

Qiu, B., Chen, S., Klein, P., Wang, J., Torres, H., Fu, L.-L., & Menemenlis, D. (2018). Seasonality in transition scale from balanced to unbalanced motions in the world ocean. *Journal of Physical Oceanography*, *48*(3), 591–605. https://doi.org/10.1175/JPO-D-17-0169.1

Richardson, L. F., & Stommel, H. (1948). Note on eddy diffusion in the sea. *Journal of Meteorology*, *5*(5), 238–240. https://doi.org/10.1175/1520-0469(1948)005<0238:NOEDIT>2.0.CO;2

Roach, C. J., Balwada, D., & Speer, K. (2016). Horizontal mixing in the Southern Ocean from Argo float trajectories. *Journal of Geophysical Research: Oceans*, *121*, 5570–5586. https://doi.org/10.1002/2015JC011440

Roach, C. J., Balwada, D., & Speer, K. (2018). Global observations of horizontal mixing from Argo float and surface drifter trajectories. *Journal of Geophysical Research: Oceans*, *123*, 4560–4575. https://doi.org/10.1029/2018JC013750

Rocha, C. B., Chereskin, T. K., Gille, S. T., & Menemenlis, D. (2016). Mesoscale to submesoscale wavenumber spectra in Drake Passage. *Journal of Physical Oceanography*, *46*(2), 601–620. https://doi.org/10.1175/JPO-D-15-0087.1

Rocha, C. B., Gille, S. T., Chereskin, T. K., & Menemenlis, D. (2016). Seasonality of submesoscale dynamics in the Kuroshio Extension. *Geophysical Research Letters*, *43*, 11,304–11,311. https://doi.org/10.1002/2016GL071349

Rosso, I., Hogg, A. M., Matear, R., & Strutton, P. G. (2016). Quantifying the influence of sub-mesoscale dynamics on the supply of iron to Southern Ocean phytoplankton blooms. *Deep Sea Research Part I: Oceanographic Research Papers*, *115*, 199–209. https://doi.org/10.1016/j.dsr.2016.06.009

Rypina, I. I., Kamenkovich, I., Berloff, P., & Pratt, L. J. (2012). Eddy-induced particle dispersion in the near-surface North Atlantic. *Journal of Physical Oceanography*, *42*(12), 2206–2228. https://doi.org/10.1175/JPO-D-11-0191.1

Sandery, P. A., & Sakov, P. (2017). Ocean forecasting of mesoscale features can deteriorate by increasing model resolution towards the submesoscale. *Nature Communications*, *8*(1), 1566. https://doi.org/10.1038/s41467-017-01595-0

Savage, A. C., Arbic, B. K., Alford, M. H., Ansong, J. K., Farrar, J. T., Menemenlis, D., et al. (2017). Spectral decomposition of internal gravity wave sea surface height in global models. *Journal of Geophysical Research: Oceans*, *122*, 7803–7821. https://doi.org/10.1002/2017JC013009

Shakespeare, C. J., & Hogg, A. M. (2017). Spontaneous surface generation and interior amplification of internal waves in a regional-scale ocean model. *Journal of Physical Oceanography*, *47*(4), 811–826. https://doi.org/10.1175/JPO-D-16-0188.1

Shuckburgh, E., & Haynes, P. (2003). Diagnosing transport and mixing using a tracer-based coordinate system. *Physics of Fluids*, *15*(11), 3342–3357. https://doi.org/10.1063/1.1610471

Su, Z., Wang, J., Klein, P., Thompson, A. F., & Menemenlis, D. (2018). Ocean submesoscales as a key component of the global heat budget. *Nature Communications*, *9*(1), 775. https://doi.org/10.1038/s41467-018-02983-w

Tarshish, N., Abernathey, R., Zhang, C., Dufour, C. O., Frenger, I., & Griffies, S. M. (2018). Identifying lagrangian coherent vortices in a mesoscale ocean model. *Ocean Modelling*, *130*, 15–28. https://doi.org/10.1016/j.ocemod.2018.07.001

Taylor, J. R., Bachman, S., Stamper, M., Hosegood, P., Adams, K., Sallee, J.-B., & Torres, R. (2018). Submesoscale Rossby waves on the Antarctic Circumpolar Current. *Science Advances*, *4*(3), eaao2824. https://doi.org/10.1126/sciadv.aao2824

Torres, H. S., Klein, P., Menemenlis, D., Qiu, B., Su, Z., Wang, J., et al. (2018). Partitioning ocean motions into balanced motions and internal gravity waves: A modeling study in anticipation of future space missions. *Journal of Geophysical Research: Oceans*, *123*, 8084–8105. https://doi.org/10.1029/2018JC014438

Van Sebille, E., England, M. H., & Froyland, G. (2012). Origin, dynamics and evolution of ocean garbage patches from observed surface drifters. *Environmental Research Letters*, *7*(4), 044040. https://doi.org/10.1088/1748-9326/7/4/044040

van der Walt, S., Schönberger, J. L., Nunez-Iglesias, J., Boulogne, F., Warner, J. D., Yager, N., et al. (2014). scikit-image: Image processing in Python. *PeerJ*, *2*, e453. https://doi.org/10.7717/peerj.453

Wagner, G. L., & Young, W. R. (2016). A three-component model for the coupled evolution of near-inertial waves, quasi-geostrophic flow and the near-inertial second harmonic. *Journal of Fluid Mechanics*, *802*, 806–837. https://doi.org/10.1017/jfm.2016.487

Wang, Y., Beron-Vera, F., & Olascoaga, M. (2016). The life cycle of a coherent Lagrangian Agulhas ring. *Journal of Geophysical Research: Oceans*, *121*, 3944–3954. https://doi.org/110.1002/2015JC011620

Wang, J., Fu, L.-L., Qiu, B., Menemenlis, D., Farrar, J. T., Chao, Y., et al. (2018). An observing system simulation experiment for the calibration and validation of the surface water ocean topography sea surface height measurement using in situ platforms. *Journal of Atmospheric and Oceanic Technology*, *35*(2), 281–297. https://doi.org/10.1175/JTECH-D-17-0076.1

Wang, Y., Olascoaga, M. J., & Beron-Vera, F. J. (2015). Coherent water transport across the South Atlantic. *Geophysical Research Letters*, *42*, 4072–4079. https://doi.org/10.1002/2015GL064089

Waugh, D. W., & Abraham, E. R. (2008). Stirring in the global surface ocean. *Geophysical Research Letters*, *35*, L20605. https://doi.org/10.1029/2008GL035526

Waugh, D. W., Abraham, E. R., & Bowen, M. M. (2006). Spatial variations of stirring in the surface ocean: A case study of the Tasman Sea. *Journal of Physical Oceanography*, *36*(3), 526–542. https://doi.org/10.1175/JPO2865.1

Waugh, D. W., Keating, S. R., & Chen, M.-L. (2012). Diagnosing ocean stirring: Comparison of relative dispersion and finite-time Lyapunov exponents. *Journal of Physical Oceanography*, *42*(7), 1173–1185. https://doi.org/10.1175/JPO-D-11-0215.1

White, M. (2018). Carl Wunsch and the rise of modern oceanography. ForecastPod.

Zhang, Z., Wang, W., & Qiu, B. (2014). Oceanic mass transport by mesoscale eddies. *Science*, *345*(6194), 322–324. https://doi.org/10.1126/science.1252418

Zhurbas, V., & Oh, I. S. (2004). Drifter-derived maps of lateral diffusivity in the Pacific and Atlantic Oceans in relation to surface circulation patterns. *Journal of Geophysical Research*, *109*, C05015. https://doi.org/10.1029/2003JC002241